Coherent interactions and thermometry in a trapped ion quantum simulator

by

Anthony Vogliano

A thesis
presented to the University of Waterloo
in fulfillment of the
thesis requirement for the degree of
Master of Science
in
Physics (Quantum Information)

Waterloo, Ontario, Canada, 2022

Author's Declaration

I hereby declare that I am the sole author of this thesis. This is a true copy of the thesis, including any required final revisions, as accepted by my examiners.

I understand that my thesis may be made electronically available to the public.

Abstract

Quantum simulators are useful tools to study exotic systems which may be otherwise intractable for a traditional computer. In particular, the trapped-ion platform has been a leading candidate for use in quantum simulation experiments because of its high fidelity state-preparation and measurement operations and its all-to-all connectivity. The relative difficulty of interacting with the long lived hyperfine states of ^{171}Yb$^+$ ions make them excellent choices for encoding information as the isolation creates stability against a noisy environment. Maintaining coherence for such a long time opens the door for complex coherent interactions, which are a backbone of quantum simulation experiments. One of the most critical coherent operations for a trapped-ion quantum simulator is the entangling Molmer-Sørenson interaction.

Building up to the Molmer-Sørenson interaction requires fine control over not just the state of the quantum register, but also the motional state of the ion. For this reason, cooling to near the ground state of motion is crucial to obtaining high fidelity experiments. Characterizing the temperature in such systems can prove challenging, requiring coherent techniques.

In this thesis, I describe my work towards preparing a Molmer-Sørenson interaction for a ^{171}Yb$^+$ trapped ion quantum simulator. I detail the methods used to bring-up the coherent Raman interactions, and characterize the Doppler cooling and Continuous Sideband Cooling (CSBC) techniques we use, their implementations on our system, and their limitations. I characterize the temperature of our ions before and after CSBC using coherent methods, showing a 46x improvement in the motional state population and confirming that post-CSBC the ions are in the Lamb-Dicke regime. I also summarize my efforts in constructing a future "blade trap" system with enough precision in the alignment of the electrodes to eventually enable efficient cooling. I show preliminary evidence that 5um precision in blade position should be feasible.

Acknowledgements

I would like to thank my supervisor Dr. Kazi Rajibul Islam for his dedication to myself and the other students of the QITI lab. Through our conversations, my knowledge and appreciation of physics has broadened and deepened farther than I could ever have expected.

I would like to thank my other committee members Dr. Alan Jamison and Dr. Michal Bajcsy for their time and helpful recommendations during my committee meetings.

I would like to thank Dr. Crystal Senko for her introductory course on trapped ions. My trapped ion literacy was greatly improved because of it, enabling me to start contributing to research as soon as I arrived in Canada.

I would like to thank the other members of the QSim lab: Sainath, Nikhil, Gilbert, Darian, Monica, Lewis, and the many co-ops that came through our doors. I would especially like to thank our post-doc Roland, who took me under his wing when I first arrived, and taught me to speak up and ask questions without embarrassment or fear of getting something wrong.

I would like to thank the students of QuantumIon and Qudit lab: Noah, Yvette, Pei Jang, Hawking, Brendan, and especially my roommate Ali for stimulating discussions on many topics.

I would like to thank Dr. Hartmut Haeffner at UC Berkeley. Without his guidance, I would never have set foot in Waterloo.

I would like to thank Mom, Dad, Emma and Zack for their support and love, without which this thesis would have been impossible.

Dedication

I dedicate this thesis to my parents.

Table of Contents

List of Figures

Chapter 1

Introduction

As physicists learn more about the world, the questions we seek to answer naturally become more complex. Indeed many problems which seem simple at first glance, like factoring numbers or determining how to wrap amino acids into a protein, can prove to be some of the hardest to solve. While classical computation has yet to provide efficient solutions to such problems and more, advancements in quantum science open the door to new problem-solving tools. Richard Feynman proposed the use of quantum mechanical systems to examine other systems, thus turning an experiment into a computer[3]. This is the basic idea of a quantum simulator. Rather than using a classical computer to simulate the behavior of a quantum system which grows exponentially more complex with system size, we can use a well-controlled quantum system with tunable parameters to serve as a representation of the system of interest. The quantum simulator in this way serves as a re-expression of the quantum system of interest, and innately scales in complexity better than a classical simulator due to its quantum nature. Many simulations today explore quantum spin models, which are composed of a sequence of two-level quantum objects, here simply called spins. Plenty of interesting physics can be investigated through studying the behavior of such quantum spin models under the effects of different interaction laws between the spins, different external forces, and other such components determining the system's evolution.

Since Feynman, many proposals for quantum information processing platforms have been explored, including superconducting circuits, photonic circuits, NMR, and NV diamond centers. Trapped ions are one of the premier platforms for this discussion because of their stability, controllability, and excellent preparation and readout processes. Furthermore, all ions of a given isotope are fundamentally identical, so instrumentation can in principle be tuned very accurately. In particular, experiments using the hyperfine levels of

^{171}Yb^{+} are well explored and offer long coherence times [4]. More information on the benefits of this particular isotope are described in Chapter 2. Through the use of a Paul trap (see Chapter 2) ions are confined to a small region in space and arrange themselves into a chain, as seen in fig 1.1. When trapped in this configuration, the ions interact through the coulomb force, forming modes of the chain.
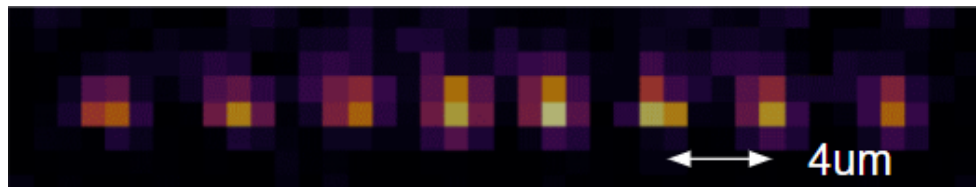
Figure 1.1: 8 ions in our trap with mean separation around 4μm. Fluorescence collected in the UV and re-colorized.

Clearly, through use of two levels of the ^{171}Yb^{+} ion as qubit levels, this setup serves as a good platform for modeling quantum spin systems. Interactions between ions can be mediated by the coulomb force, and other factors in the system evolution can be introduced through external optical/near UV addressing, B-fields, etc.

Single ions are useful for characterizing a system, serving as a highly-sensitive detector for our control methods, but to fully utilize the power of multiple ions in our trap, we require a method of generating entanglement, else we simply have a collection of single qubits. In trapped ions, one especially prominent method of generating entanglement is by way of the Molmer-Sørenson (MS) interaction. The MS interaction utilizes the collective motional modes of the chain to generate spin-motion coupling. When applied correctly, the spin-motion coupling closes it's loop in phase space, which is to say that the spin-motion coupling returns the ions to their original state. However, the resultant spin-spin coupling can be non-zero. To successfully implement this operation, we must be particularly resistant to unwanted shifts both in the qubit state as well as its motion, since both are involved in the mechanism. This is best satisfied when the ions are very cold relative to their confining potential. Fundamental limitations on Doppler cooling require that for our current trapping conditions, further cooling methods are required. Moreover, characterizing the temperature of such cold ions requires the use of coherent techniques.

In this thesis, I intend to discuss my progress in building up the experimental system to implement this using the building blocks for this complex coherent operation, and perform thermometry on our ^{171}Yb^{+} ions after cooling below the Doppler limit.

1.1 Outline

The following is the brief outline of the structure of this thesis

- In Chapter 2, I discuss some fundamental physics of trapped ions as a platform, the origin of micromotion, and also some broad strokes regarding the Molmer-Sørenson protocol and the temperature requirements to run it efficiently.

- In Chapter 3, I describe the basics of how we use ^{171}Yb$^+$ as our qubit, how we stabilize our lasers for a two-photon process, and how we begin to overlap them.

- In Chapter 4, I detail the methods in which we use the experiments with the ion to advance our progress towards the MS protocol, and characterize our system along the way.

- In Chapter 5, I discuss my project preparing to align blade electrodes for our new setup, and lay out the reasoning for my alignment goals.

- Chapter 6 concludes this thesis with some ideas about related topics for future work.

Chapter 2

Background Physics

In this chapter, I will review some of the physics which will be used in later in this thesis. First, I will explain the method by which we are able to trap ions in the first place, and how it relates to the origin of micromotion. Then I will discuss coherent interactions in the two level atom, which will be used to explain the phenomena we observe in Chapter 4 and motivate the design I describe in Chapter 3.

2.1 Trapping and Micromotion

In order to obtain localized ions for use in quantum simulation, we must find a way to create a local potential minimum. While we cannot create a local extremum with electrostatic fields (Earnshaw Theorem), we can create a time-averaged potential minimum by utilizing RF electric fields. For our initial description of the potentials, I will utilize a simplified picture of our four-rod trap setup, where four equally sized and spaced rods of approximately infinite length (relative to the ions) are arranged such that the RF drive on opposite rods are in-phase and the nearest rods are 180° out of phase. The cross section for our setup with drive RF at Ω_R can be seen in fig. 2.1.
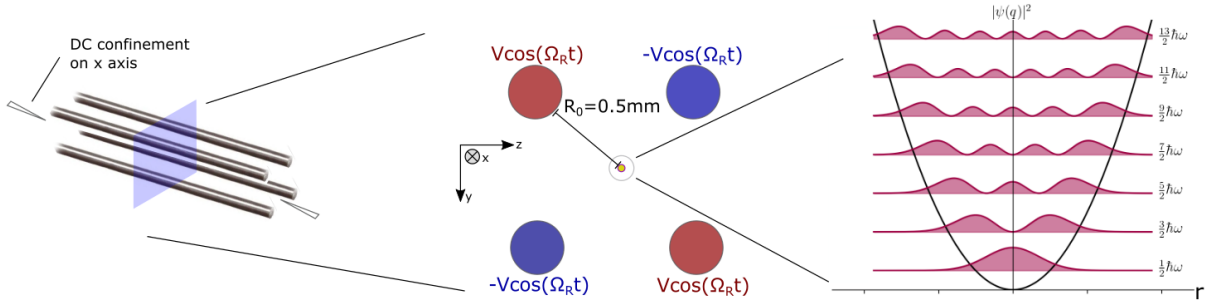
Figure 2.1: Four rods provide RF voltages while needles provide DC. The average force felt by the ion approximately describes a harmonic pseudopotential.

The potential created using equal magnitude but opposite phase electrodes (also assuming that the shape of the electrodes is hyperbolic, which is close to the circular rods we use), is a saddle potential [2]:

$$V(x, y) = \alpha(x^2 - y^2)\cos(\Omega t) \tag{2.1}$$

The time average of this saddle potential is zero, with zero field at the null point. Removing the oscillating term, it is clear that the potential is not confining, but at best simply flat. However, a few approximations will show us that this configuration can create an *effective* potential.

2.1.1 Pseudo-potential derivation

This derivation follows closely to a work published by Gerlich [5]. Consider first a charged particle in an EM field. It's motion will be described by

$$m\ddot{\mathbf{r}} = q\mathbf{E}(\mathbf{r}, t) \tag{2.2}$$

where we have ignored all contributions of $\dot{\mathbf{r}} \times \mathbf{B}$ since our particle is moving slowly and the magnetic field is not strong. Let us assume that the field is homogeneous, varying only with time, and that the field is purely RF, with no static component. For an example of this, consider the field inside of a large parallel plate capacitor, where the field will lie along the axis normal to the plates. This turns our differential equation into a one dimensional problem:

$$m\ddot{\mathbf{r}} = qE_0\cos(\Omega t)\hat{\mathbf{j}} \tag{2.3}$$

which is solved by

$$\mathbf{r} = -\frac{qE_0}{m\Omega^2}\cos(\Omega t)\hat{\mathbf{j}} = \mathbf{a}\cos(\Omega t) \tag{2.4}$$

where the amplitude of oscillation is wrapped into the variable

$$\mathbf{a} = -\frac{q\mathbf{E}_0}{m\Omega^2} \tag{2.5}$$

for convenience. A particle with a small linear velocity would also represent a valid solution, with these oscillations at Ω acting as excursions about the linear trajectory. The important note here is that this amplitude goes as Ω^{-2}. The case we seek to study is clearly inhomogeneous though, so let's adapt this solution to describe that case. Let's look at the first order Taylor expansion of the electric field at a point $\mathbf{r}_0$.

$$\mathbf{E}(\mathbf{r}, t) \approx \mathbf{E}(\mathbf{r}_0)\cos(\Omega t) + (\mathbf{r} - \mathbf{r}_0) \cdot \nabla \mathbf{E}(\mathbf{r}_0)\cos(\Omega t) \tag{2.6}$$

Where on the right hand side I have broken up the Electric field into it's spatial and time dependent parts. Again, we understand that the electric field will exert a force on our charged ions, according to

$$m\ddot{\mathbf{r}} = q\mathbf{E}(\mathbf{r}, t) = q\mathbf{E}(\mathbf{r}_0)\cos(\Omega t) + q(\mathbf{r} - \mathbf{r}_0) \cdot \nabla \mathbf{E}(\mathbf{r}_0)\cos(\Omega t) \tag{2.7}$$

We shall say that the motion $\mathbf{r}$ is defined in terms of some fast varying component $\mathbf{r}_f$ and some slow varying component $\mathbf{r}_s$.

$$\mathbf{r}(t) = \mathbf{r}_f(t) + \mathbf{r}_s(t) \tag{2.8}$$

The fast oscillations are what we found earlier in the homogenous case, and are at the trap frequency.

$$\mathbf{r}_f(t) = \mathbf{a}(t)\cos(\Omega t) \tag{2.9}$$

where again $\mathbf{a}$ defines the amplitude of fast oscillations about the slow path defined by $\mathbf{r}_s$. However, now we assume that $\mathbf{a}$ will vary over space (it remains time independent in the sense that the geometry of the fields are not varying, but the particle may move around). Also, we assume that our RF drive is fast enough that the amplitude of $\mathbf{a}$ is small, at least with respect to the variation in the electric field over that distance. Therefore, the ion's motion will be described by some fast but small oscillations about some slow but large trajectory. The amplitude of the small oscillations $\mathbf{a}$ does change in time with the slow trajectory, so it varies slowly with respect to the drive frequency: $\dot{\mathbf{a}} \ll \Omega\mathbf{a}$. Let us consider at a given moment t' that $\mathbf{r}_s(t') = \mathbf{r}_0$. This would then give us

$$m(\ddot{\mathbf{r}}_s + \Omega^2\mathbf{a}(t)\cos(\Omega t)) = q\mathbf{E}(\mathbf{r}_0)\cos(\Omega t') + q[\mathbf{a}(t) \cdot \nabla \mathbf{E}(\mathbf{r}_0)]\cos^2(\Omega t') \tag{2.10}$$

6

where if we look back at the scaling for $\mathbf{a}$, we find that the second term on the left hand side and the first term on the right hand side cancel. Expanding $\mathbf{a}$, we are left with

$$m\ddot{\mathbf{r}}_s = -\frac{q^2}{m\Omega^2}[\mathbf{E}(\mathbf{r}_0) \cdot \nabla \mathbf{E}(\mathbf{r}_0)]\cos^2(\Omega t') \tag{2.11}$$

I will use the identity

$$\mathbf{E} \cdot \nabla \mathbf{E} = \frac{1}{2}\nabla \mathbf{E}^2 - \mathbf{E} \times (\nabla \times \mathbf{E}) = \frac{1}{2}\nabla \mathbf{E}^2 \tag{2.12}$$

in the quasi-static approximation, and also approximate the fast oscillations out:

$$\cos^2(\Omega t) \approx \frac{1}{2} + \cos(2\Omega t)/2 \approx 1/2 \tag{2.13}$$

which finally yields

$$m\ddot{\mathbf{r}}_s = -\frac{q^2}{4m\Omega^2}\nabla \mathbf{E}^2 \tag{2.14}$$

as the equation of motion. This form bears a striking resemblance to the equation

$$m\mathbf{a} = -\nabla U \tag{2.15}$$

. In this way, we can see that the motion of our ion will look similar to that of the motion of a particle in a potential described by a 'pseudo-potential' that goes as:

$$F_{avg} = -\nabla \frac{q^2 E^2(r)}{4m\Omega^2} \tag{2.16}$$

and while the saddle potential does not have minima, the square of the electric field acting as an effective potential has a minimum at the saddle point.

$$E^2 = \alpha(x^2 + y^2) \tag{2.17}$$

and the parabolic shape of this pseudo-potential informs us that the motion of the particle will be that of a harmonic oscillator. Note that the characteristic frequency of the harmonic oscillator is not the drive frequency but rather

$$\omega \approx \frac{V}{\sqrt{2}m\Omega R_0^2} \tag{2.18}$$

called the "secular" frequency. The motional state of the ion inside the harmonic potential can be characterized in terms of its phonon number. We will later use the phonon modes of

this system in our coherent interactions. In the absence of stray electric fields, the particle will stay near the center of the harmonic oscillator. The fast oscillations at Ω detailed in the derivation demonstrate the non-harmonic component of the motion (which has frequency at the drive frequency, not the secular frequency). This motion is called micromotion. Even when the ion is completely in the ground phonon state, the wavefunction still spreads out a small distance, so there will always be some "intrinsic" micromotion. However, if the ion's equilibrium position is shifted away from the center of the harmonic potential, say by some stray electric field, then there will be an additional micromotion called "excess" micromotion. Excess micromotion can induce heating through coupling to the phonon modes. If the classic trajectory of a charged particle is simulated in this configuration, it can be seen that the intrinsic micromotion corresponds to motion with frequency $\Omega_R \pm \omega$ while the excess micromotion occurs at Ω_R [1].
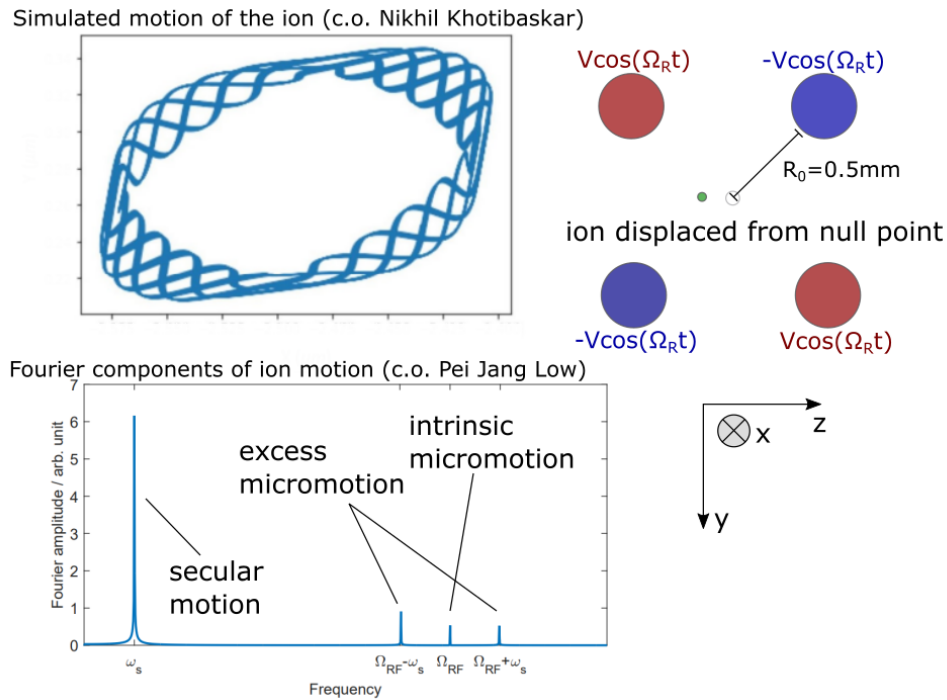

Figure 2.2: Induced micromotion of a charged particle trapped in a Paul trap.[1][2]

Micromotion can induce heating through coupling to one of the phonon states of the harmonic potential. Micromotion compensation is the process by which we minimize the excess micromotion to reduce this heating. One reason we are particularly concerned about

this heating is that it is omnipresent whenever an ion is in the trap, even mid-experiment. For experiments where preserving the phonon state is critical, micromotion minimization is an important step in reducing noise. For our experiment, we are able to utilize a 4MHz linewidth transition in the $^2D_{3/2}$ repump process for $^{171}Yb^+$ to scan for the micromotion. Once the transition is found, we can detect sidebands on this transition at a frequency of Ω_R away, corresponding to the detuning where a micromotion heated ion observes a doppler shifted light on resonance. To perform the micromotion compensation from here, I adjust the DC bias voltages of the four rods to minimize the amplitude of this sideband, corresponding to a reduction in the heating rate.

2.2 Atomic transitions

When we have a two level atomic system interacting with a classical electric field, we may drive transitions between the two states when the field is tuned near the frequency separation of the eigenstates. The rate of this transition scales according to the dipole operator of the atom and the strength of the electric field,

$$\Omega = -\frac{\langle\downarrow|\,\hat{\epsilon}\cdot\mathbf{d}\,|\downarrow\rangle\,E_0}{\hbar} \tag{2.19}$$

and is called the Rabi rate. Here Ω is the Rabi rate, $\hat{\epsilon}$ is the polarization of the electric field of magnitude E_0, with $\mathbf{d}$ as the dipole operator. The dipole operator represents the susceptibility of the ion to polarize in the presence of a strong electric field, or alternatively, how tightly the position of the negatively charged electron is bound to the positively charged nucleus. When the frequency is detuned from resonance, we observe instead a modified Rabi rate

$$\widetilde{\Omega} = \sqrt{\Omega^2 + \Delta^2} \tag{2.20}$$

which is the quadrature average of the resonant Rabi rate and the detuning, Δ [6]. If instead we seek to drive a transition using two fields, in a Lambda-type system, then the overall transition rate will be

$$\Omega = \frac{\Omega_1 \Omega_2}{2\Delta} \tag{2.21}$$

where the detuning here is the detuning of both lasers from the excited state. This detuning is necessary in order to eliminate population transfer to the excited state, so in general we want to pump as much power into the laser light as possible to increase this two-photon Rabi rate [7].
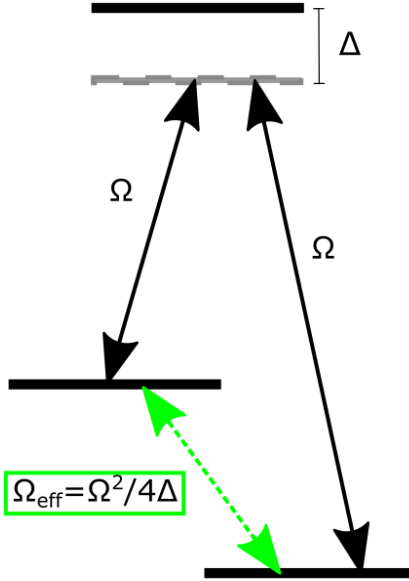
Figure 2.3: Lambda-system for two photon Rabi oscillations. In our experiment, the single photon Rabi frequency for both beams are approximately equal.

Why are we interested in this model? The Molmer-Sørenson interaction [8] is a simple entangling operation which we can use, requiring one red-detuned and one blue-detuned transition (for the base case). A picture of the energy levels is drawn in fig. 2.4. When extending to multiple ions in the trap, the phonon number is replaced by a mode structure, increasing the complexity of the diagram somewhat. However, these modes aren't as far apart in energy as they are to the carrier transition, so I draw them as one level here. In practice, we park our detuning so that the main contributing mode will be the tilt mode, which is on the edge of the mode forest.
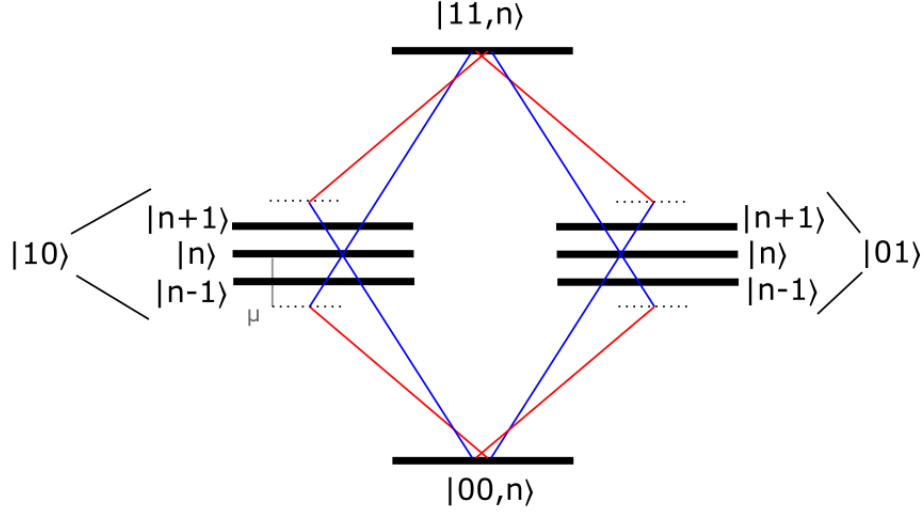
Figure 2.4: Level diagram of the transitions driven by the Molmer-Søresonson protocol. Note that only two different sideband frequencies are required due to symmetry, but that each transition is a two-photon transition.

One key target for ensuring that the Molmer-Sorenson protocol functions well is that we are operating in the Lamb-Dicke regime. The Lamb-Dicke parameter (η) is used to determine where this regime falls and is characterized

$$\eta = kx_0 = \frac{2\pi}{\lambda}\sqrt{\frac{\hbar}{2m\omega}} \tag{2.22}$$

as the product of the ground state wavefunction spread and the wavenumber of the laser beam. For a two-photon process, the wavenumber of the beam is replaced by the difference in the beam's k-vectors, $\Delta\mathbf{k}$. For a multi-ion process, eta is modified to include the mode participation as well:

$$\eta_{i,m} = \Delta\mathbf{k}\sqrt{\frac{\hbar}{2m\omega}}b_{i,m} \tag{2.23}$$

where $b_{i,m}$ is the mode participation of ion i in mode m. The Lamb-Dicke parameter is dimensionless, but can be thought of as a measure of the size of the ion. This parameter also defines the relative strength of our sideband transitions, which is why we cannot use a microwave single-photon process for this system - the sideband strengths for microwave are four orders of magnitude weaker meaning the sidebands are almost invisible.

11

We are in the Lamb-Dicke regime when the condition

$$\eta^2(2\bar{n} + 1) \ll 1 \qquad (2.24)$$

is satisfied, which corresponds to the regime where coupling between the qubit state and the harmonic oscillator state is exponentially suppressed [9].

$$H \approx \text{Carrier} + \underbrace{\boxed{\eta\text{RSB}} + \boxed{\eta\text{BSB}}}_{\text{Want to keep}} + \underbrace{\eta^2(\text{Higher order sidebands}) + ...}_{\text{Don't want}}$$

Figure 2.5: The Lamb-Dicke regime corresponds to a small value approximation of η, where higher order terms (sidebands) are suppressed.

It is important to reside in this regime for coherent operations because we want to eliminate unwanted heating (once we start an experiment, we only want to modulate the phonon number when we desire) similarly to how we seek to minimize excess micromotion.

Generally we perform a more arbitrary transformation than the gates above, based on the evolution operator of the form [7]

$$U(t) = exp\Big(\sum_{i,m}(\alpha_{i,m}(t)a^\dagger - \alpha_{i,m}^*(t)a)\sigma_x^i + \sum_{i,j:j<i} J_{i,j}\sigma_x^i\sigma_x^j t\Big) \qquad (2.25)$$

where α determines some coupling of the qubit state to the motion (we call this spin-motion coupling) and $J_{i,j}$ determines the resultant qubit-qubit coupling that results from spin-motion coupling. In our experiment, we either make the amplitude of α small so that its contribution is negligible, or we ensure that we operate for a specific gate time that enforces all $\alpha_{i,m} \approx 0$. The form of $J_{i,j}$ is given by

$$J_{i,j} = \sum_m \frac{\Omega_i\Omega_j\eta_{i,m}\eta_{j,m}\omega_m}{\mu^2 - \omega_m^2} \qquad (2.26)$$

where Ω_i is the single ion Rabi frequency of ion i, μ is the equal and opposite detuning of the red and blue sidebands (see fig 2.4), and ω_m is the frequency of mode m. This interaction generalizes well to longer chains of ions, allows us to generate many-body entangled states easily, and can be shown (for the two qubit MS gate) to form a universal gate set when paired with other single qubit gates.

More details on coherent operations observed in this work are detailed in Ch 4, performed on the setup described next.

Chapter 3

Setup

In this chapter I will discuss more of the specifics in our implementation scheme. I will start with a brief look at the ion we use, and then shift to describing the work on the setup I did in order to enable our two-photon coherent operations.
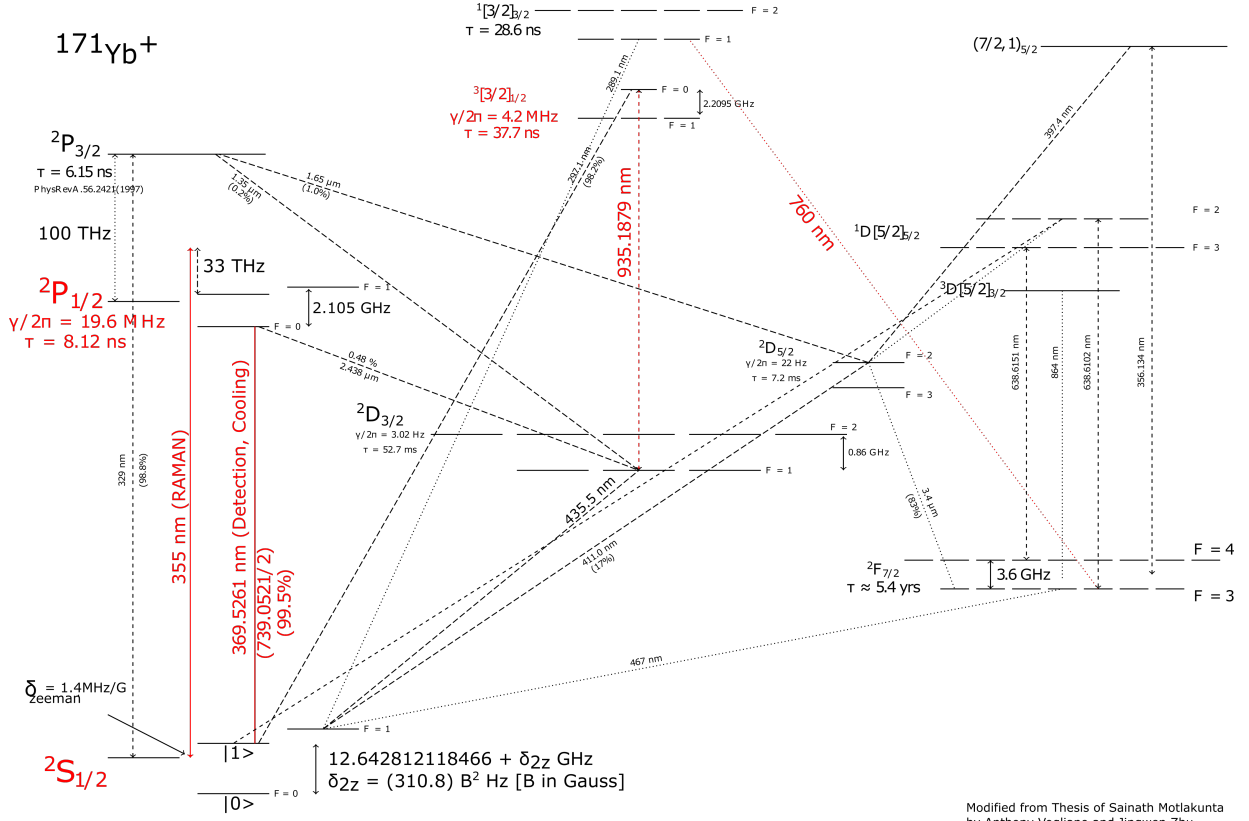
Figure 3.1: Energy structure of $^{171}\mathrm{Yb}^+$

3.1 Our ion

Our lab utilizes $^{171}\mathrm{Yb}^+$ in our experiment. A full energy diagram can be seen in fig. 3.1.

We generate the ions in our trap using a two-step ionizing transition. The Yb is fired through the center of the trap from a neutral Yb atomic oven source. With the ions generated, we use the long-lived hyperfine levels of the $2S_{1/2}$ state as our qubit states. We define our qubits as follows:

$$\left|2S_{1/2}, F = 1, m_f = 0\right\rangle = |1\rangle = |\uparrow\rangle = \text{"Bright state"} \tag{3.1}$$

$$\left|2S_{1/2}, F = 0\right\rangle = |0\rangle = |\downarrow\rangle = \text{"Dark state"} \tag{3.2}$$

14

We apply a static magnetic field in order to lift the degeneracy of the mf levels in the $F = 1$ manifold. To perform a measurement operation, 369.5nm light excites only the $F = 1$ states to the $\left|^2P_{1/2}, F = 0\right\rangle$ state, which quickly decays back to $\left|^2S_{1/2}, F = 1\right\rangle$ for which the transition to $\left|^2S_{1/2}, F = 0\right\rangle$ is forbidden. For this reason, we call $\left|^2S_{1/2}, F = 1\right\rangle$ our "bright" or "up" state and $\left|^2S_{1/2}, F = 0\right\rangle$ our "dark" or "down" state. The frequency difference between these two levels is about 12.6428 GHz, varying slightly depending on the magnetic field. The variation is insensitive to first order in the B-field, which is one beneficial trait of this choice of qubit state. Doppler cooling is performed by red-shifting the transition above, along with a 14.7 GHz sideband created by an Electro-optical modulator (EOM) to re-pump any ions that are off-resonantly excited to the $^2P_{1/2}, F = 1$ manifold, which does have an allowed transition to the dark state, as well as to the bright state. Technically, the "cycling transition" for the bright state isn't perfect, even including off-resonant excitation. There is a small chance of decaying from the $\left|^2P_{1/2}, F = 0\right\rangle$ state to another level, $\left|^2D_{3/2}\right\rangle$, where the population can be stuck for a significant time - the lifetime of the D state is longer than 50ms. For this reason, we introduce a 935nm laser to drive the population from this state into a state with a fast decay ($\tau = 37$ns) to the $\left|^2S_{1/2}\right\rangle$ manifold. For state preparation, we can replace the 14.7 GHz sideband with a 2.1 GHz sideband. This systematically empties the bright state by way of the decay from $2P_{1/2}, F = 1$ to the dark state, "optically pumping" the target qubits to the dark state. A zoomed in energy level diagram with the key energy levels in our setup is shown in fig 3.2 with the Doppler cooling light frequencies. For our usual parameters, δ is around 10 MHz.
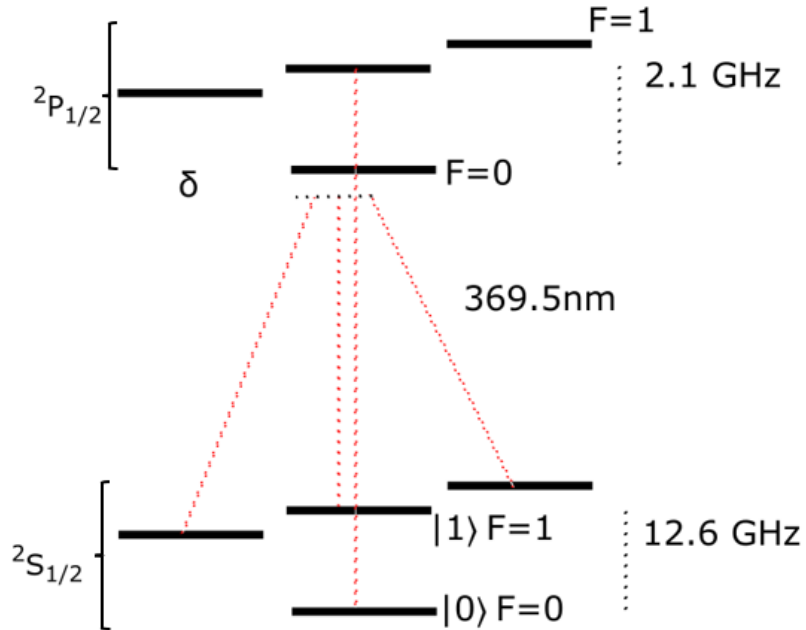
Figure 3.2: Key energy levels in our system with Doppler cooling light

3.2   Coherent Operation setup

To perform global coherent rotations, we use a HP8762A microwave source aimed at the trap center with a microwave horn (Flann 18810-QA-11316, Elettronica Spa 595.000.601). The long wavelength of the microwave disallows us from focusing onto specific ions. This is a primary motivator for moving towards the stimulated Raman transitions for our coherent pulses.

In our system, we utilize a pulsed 355nm laser from Coherent (Paladin Advanced 355-8000). As opposed to a CW laser, a pulsed laser only transmits light during discrete intervals separated by some characteristic repetition time τ. For this laser, $\tau \approx 12.45$ ns. While the repetition time is an important value, it is more useful to consider this laser from the perspective of the frequency domain. Consider the time domain signal that the laser produces on a sensor, which is a pulse train with peaks separated by 12.45 ns. The length of one pulse is around 15ps. Within this pulse are the femtosecond oscillations from the 355nm light. However, when a photodiode is used to measure the light, it will also pick off the beat notes that the pulses form with each other. I perform this measurement using

a Hammamatsu photodiode (G4176) connected to a bias tee to convert the optical signal into an RF electrical signal that can be picked up on a spectrum analyzer. I measure a frequency comb, with peaks equally spaced by 80.343 MHz. This makes sense, since the Fourier transform of a pulse train is another pulse train, with pulse separations described by the inverse of the temporal separation of the pulses. Therefore, in the frequency domain, we measure 80.34 MHz $\approx$ 1 / 12.4ns as the fundamental beat note. While the photodiode signal is usually filtered to measure a particular beat note, the ion senses all beat notes simultaneously. A sketch of this beatnote comb can be seen in fig. 3.3.
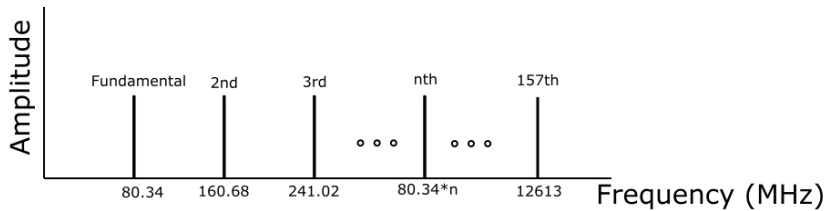
Figure 3.3: The multiple orders of beat notes measured by the ion from the pulsed laser light.

This comb will be used to drive our atomic transition. Consider for instance the 1st and the 158th order peaks, which will be separated by 80.34MHz * 157 = 12.614GHz. We can also see that the 2nd and 159th order beat notes will be separated by the exact same amount as well, as will the nth and (157+n)th. This particular value is of interest because the frequency spanned between these peaks is very close to the energy separation of our hyperfine qubit at 12.643 GHz. Consider now that we have two identical duplicates of the signal falling on the same sensor, but one of the signals is shifted in the frequency domain by some amount Δ. If we are able to tune this shift such that $\Delta = 29$MHz, then we would be able to use the beat note formed between the fundamental of one comb and the 158th comb tooth of the other comb to drive our transition. We use Acousto-optical modulators to create this detuning and achieve precisely this configuration of frequencies at the ion. The pulsed laser light is split into two paths with a UV Polarizing Beam Splitter (PBS). We apply two different frequency shifts to the comb teeth using Acousto-optical modulators (AOMs), particularly the ASM-B series from Intraaction. These devices use the acousto-optic effect to diffract the light and imprint a shift in the frequency on the diffracted beam. This allows us to not only write a frequency onto the light, but also spatially separates this from the un-modulated light, reducing background noise. These AOMs also enable fast switching times (sub μs), and provide a platform for modulation of the frequency for

spectral analysis, detailed later. As a quick note, rather than shifting only one arm by 29MHz, we shift each arm away by roughly half of 29MHz in opposite directions, so one arm will be at 186MHz and the other at 215MHz (the specs for the ASM-B series says that 40MHz shifts are possible, but efficiency is maximized near 200MHz). Both sides use the $+1^{st}$ order diffraction, obtaining at least 70% efficiency and picking off the other orders using a D-mirror to reduce background.

However, the cornerstone of the above description is the repetition time. If τ was to have some uncertainty or drift in time, then there would be a corresponding shift in the spacing of the frequency comb, which would break the frequency difference between these combs of interest. These fluctuations are much slower than the repetition time, occurring on the order of tenths of seconds, so we can assume that the corresponding shift in the repetition rate defines the spacing for the entire comb. A primary drift in the system for the repetition time is due to thermal fluctuations of the laser head, for example. This is illustrated in fig 3.4.
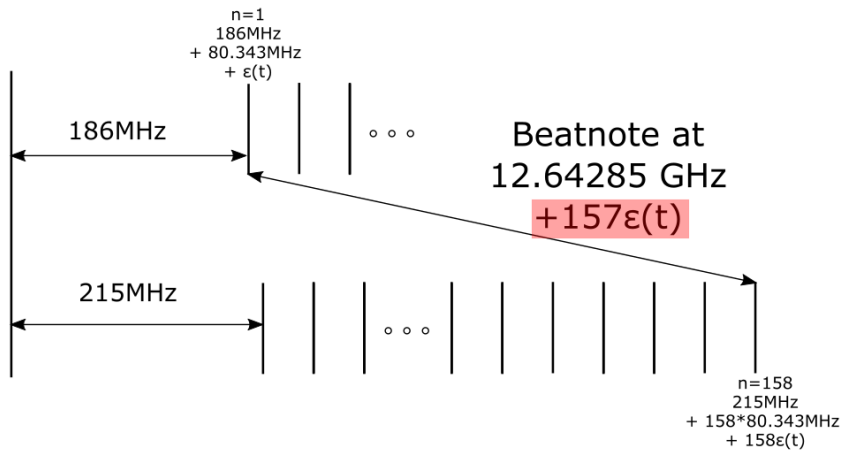
Figure 3.4: The transition only matches the hyperfine transition for certain points in time. Stabilization is required.

Feeding back onto the laser controls would solve this issue, but we do not have access to these parameters for our setup, so we require an external solution. To correct for these time dependent errors, I replaced one of the arms of the setup above with a time dependent frequency shift, where the signal is generated by a Phase-locked loop (PLL) (Analog Devices ADF4355).

The PLL circuit takes a measurement of the frequency comb and uses its drift to

continuously adjust the frequency of the output. Therefore, we are able to continuously pass a signal to the AOM and compensate for the drift in the other comb. The end result is that while the spacings of the comb teeth shift over time, the difference between the comb teeth of interest (the fundamental and the 158th) will be constant over time, as shown in fig. 3.5.

n=1
186MHz
+ 80.343MHz
+ 158ε(t)

186MHz + 157ε(t)

Beatnote at
12.64285 GHz

215MHz

n=158
215MHz
+ 12694.194MHz
+ 158ε(t)
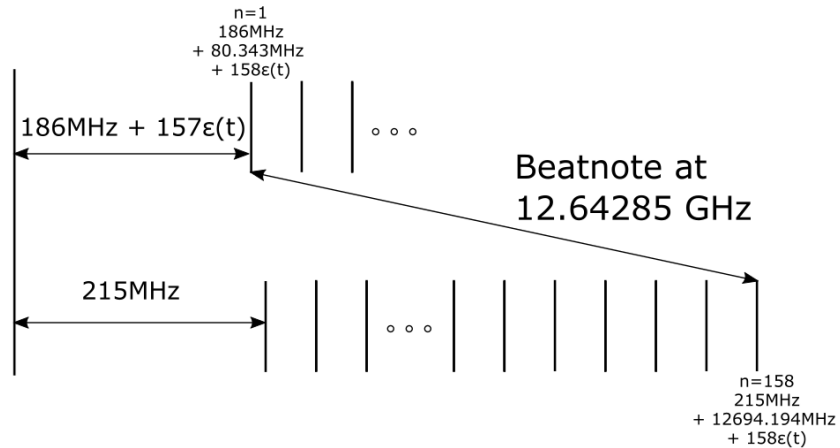
Figure 3.5: Configuration of the beat note combs that can drive the hyperfine transition

LO
79.16MHz

LPF
$f_{rep}(t)$

LPF
1.185MHz + ε(t)

PLL
*157

AOM
186MHz + 157ε(t)
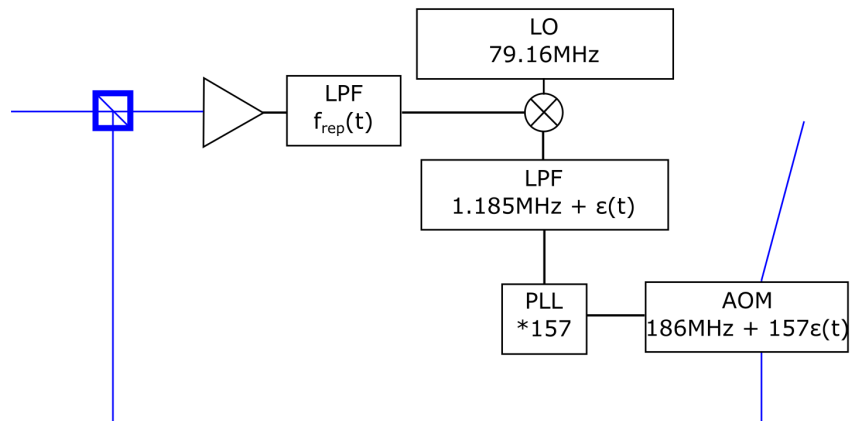
Figure 3.6: Configuration of the beat note lock electronics

I assembled the phase locked loop circuit sketched in 3.6. This circuit uses the filtered signal of a photodiode observing the 355nm pulsed beam. The first filter removes all but

19

the first few comb teeth from the signal, since we will be using the fundamental as our locking comb tooth. In principle, the setup below can be re-done for another comb tooth, assuming the settings are adjusted accordingly. For this description, we will assume that the fundamental's frequency as a function of time is $f(t) = 80.343\text{MHz} + \delta(t)$ with $\delta(t)$ acting as the error signal. $\delta(t)$ is typically on the order of a few kHz, and drifts within an approximately 20kHz-width-range, as measured by taking the max and min values over an hour-long period. Short term fluctuations are usually a few hundred Hz per second. The filtered signal is then mixed with a RF source (Rigol AWG DG4102) locked to a 10MHz atomic reference (SRS FS725). The frequency of this RF source is selected such that when the laser is precisely at the 80.343MHz average rep-rate value, the mixer outputs the desired frequency for the AOM, divided by the ratio of the beat note indices. In our case, this is simply $80.343\text{MHz} - 186\text{MHz} * \frac{1}{157} \approx 79.16\text{MHz}$, which means the mixer down-converts to 1.185 MHz, modulated by $\delta(t)$. The second filter removes all but the lowest mixed frequency, which is the down-converted signal we want. This signal is fed to the PLL, which with our setup acts like a frequency multiplier. With $1.185 + \delta(t)$ MHz as the reference signal, the PLL outputs $\left(1.185 + \delta(t)\text{MHz}\right) * 157 \approx 186 + 157\delta(t)$ MHz. The PLL outputs around -20dBm of power. The output of the PLL is connected to an attenuation board (PE4312) and other static attenuators for power control and to ensure the signal is never beyond the safety limit of the AOM (usually 10dBm). This is passed to a low noise pre-amplifier (ZFL-500LN+, +28dB), then a high power amplifier (MPA-40-40, +36dB) for a total RF power at the AOM of around +36 dBm, or 3W. A schematic can be seen in fig 3.7.
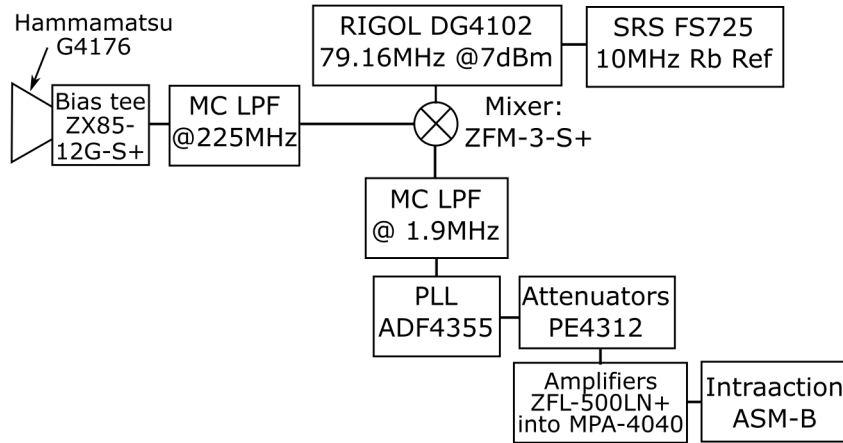
Figure 3.7: Details of electrical connections for the beatnote stabilization circuit

The inside of the PLL can be thought of as three separate components: a counter, a charge pump, and an oscillator. The counter measures and compares the rising and falling edges both of the input and the output. The charge pump modulates an output voltage based on the comparison, and the oscillator continuously modulates its frequency without adjusting the absolute phase. A simple sketch is shown in fig 3.8.
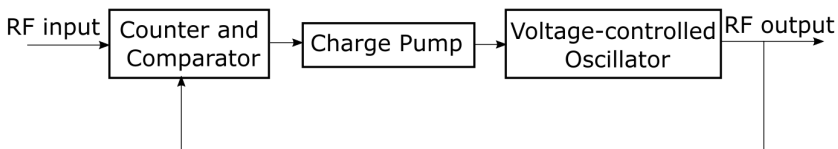
Figure 3.8: Simplified drawing of the internal mechanism of the PLL. It functions essentially as an RF source using the RF input as a stable reference, but because our RF source is not in fact stable, the RF output will modulate by the ratio we specify.

Each of these components has many options, and while I will refrain from describing all of the settings, a challenge of this work was to parse all of these controls and determine how best to optimize our implementation. A sample of a settings menu can be seen in 3.9.
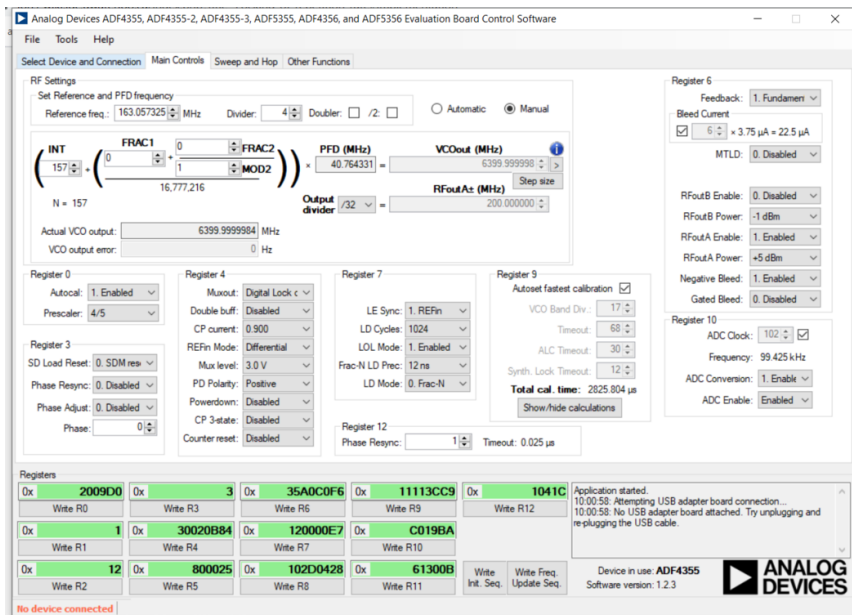
Figure 3.9: Settings menu for programming the PLL

The final output of the PLL is amplified and passed on to the AOM, at which point it becomes part of the greater Raman optics setup.

3.2.1   Path-length matching

Because we are driving a two-photon transition, we require both photons to be coincident at the ion for the transition to occur. The pulses of the laser therefore need to be overlapped both in space and in time at the ion. With both of the beams coming from the same split source, we must ensure that the path lengths from the split to the ion are exactly matching in order to satisfy this condition. The pulses from our laser are 15 ps long, so in space they are 4.5mm long. To perform initial path-length matching, I measured the full distance travelled by the two beam paths from the beam splitter using a ruler. With both paths only a few millimeters off (roughly measured), I aligned a beam into a pair of mirrors on a translation stage. With the incoming beam roughly parallel to the table, and shifting the translation stage back and forth, I ensured that the twice reflected beam height matched the beam height from the mirror preceding the translation stage. Then, I ensured that the beam travelled along the screw holes of the optics table itself, matching the input beam. With both of these conditions satisfied simultaneously, through the full translational distance of the delay stage, I could ensure that the axis of the stage, the input beam, and the output beam were all parallel. With this in place, I was able to adjust the total length of the Raman path without affecting the other optics in the system. This is important since the path length matching is one of the last knobs to turn when optimizing the Raman signals described in Ch. 4, so adjusting it can't be allowed to affect the rest of the system.
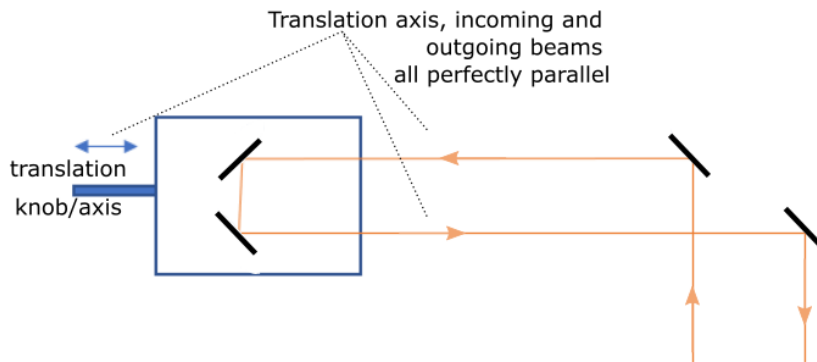
Figure 3.10: Raman path-length matching stage

3.2.2 Full Raman Setup
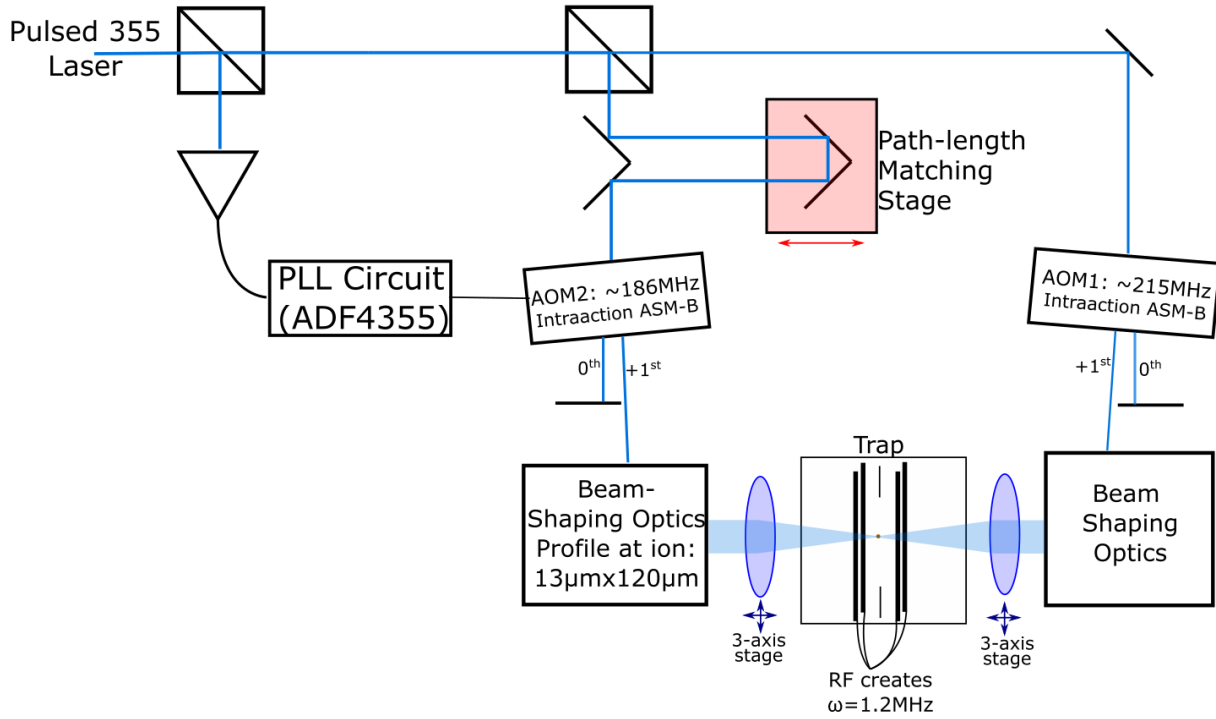
Figure 3.11: Raman optics and electronics setup

The full Raman setup is shown in fig 3.11. The beam shaping optics simply squeeze the modulated beam from the AOM to be narrow perpendicular to the ion chain and wide parallel to the ion chain, forming a beam with waists of 13 μm and 120 μm respectively (after passed through the final 100mm lens). The beam shaping is composed of a sequence of telescopes. An initial cylindrical mirror creates the mismatch in the waists along the two axes. A mirror is located at the intermediate image plane (IIP) to allow for slight adjustments in the tilt of the beam at the ion plane.
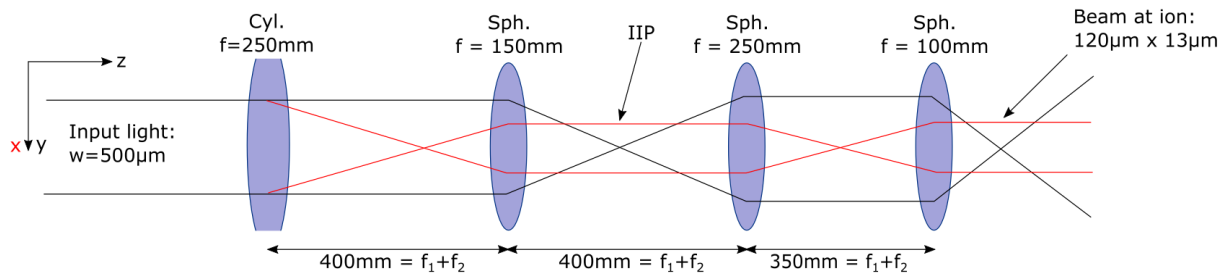
Figure 3.12: Raman beam shaping unwrapped.

The final lenses on both sides are mounted to a 3-axis Newport translation stage. When the incoming beam is displaced a small amount from the from the center of this lens, the beam at the focus should shift by an equal amount. This acts as our fine alignment knob to get the position of the beams perfectly overlapping at the focus at the ion position. This knob, along with the path-length match knob are the two that will be used during the first coherent interactions to optimize the spatial and temporal alignment of the two beams.

Chapter 4

Ion Signals

In this chapter, I will describe the signals we observe from our ion which we use to measure and verify our coherent operations. For each experiment below, the sequence of operations is 1) Cool 2) Initialize 3) Operate 4) Measure. All fluorescence counts in this chapter correspond to light captured on a photo-multiplier tube (PMT) focused and aligned to the ions. While all data within a given plot is consistent, the detection time, detection power, and other such parameters are re-calibrated frequently and therefore the number of counts between plots should not generally be compared with one another. However, values of fluorescence for a single bright state ion in these experiments usually range from 6 to 12 counts. During Raman experiments, roughly 0.5W of optical power is used along each Raman path, calibrated via a $\lambda/2$ waveplate before the PBS that splits the Raman paths.

4.1 Ramsey Alignment

Before performing any qubit physics, I first roughly aligned the Raman beam to the center of the apparatus by imaging the rods and needles. For the optical axis, I was able to use the clipping of the beam on the rods (along with the information of which direction I was moving the translation stage) to determine which side of the focus I was on. When both sides of the beam were clipping equally, I could confirm that the focus was roughly at the center. With the beam aligned as best as I could using my optics toolbox, I then used Ramsey measurement to determine the optimum alignment position. This method relies upon the AC Stark shift, wherein the light is considered a perturbation on the system Hamiltonian, and the new states have shifted energy levels. Larger intensities of light correspond to larger shifts in the energy levels. The maximum Stark shift we can observe

for our setup is the 4th order Stark shift, which scales as the square of the intensity of the incoming beam (or the fourth exponent of the electric field, E^4). The two photon Rabi rate we will find later, on the other hand, is proportional to the product of the E-fields from the two Raman paths. The Raman lasers incident on the ion are (ideally) Guassian beams of waist 13μm by 120μm. One waist unit away from the center corresponds to a drop in the electric field by a factor of e, so we expect a fourth order Stark shift to provide a sensitive measurement for alignment - one waist away will drop the stark shift by roughly 50. The Stark shift effect is also able to be used with only a single beam path, since we aren't actually seeking to drive a resonant transition. The stabilization of the frequency comb doesn't matter here, since the detunings are already very large (Many MHz), so KHz drifts are insignificant. The 4th order differential Stark shift is maximized when the light is of perfect σ polarization with regards to the ion's polarization axis (the magnetic field direction), so a $\lambda/4$ waveplate is added at the final lens.

In a typical Ramsey experiment on our setup, two microwave $\pi/2$ pulses from the same source are spaced apart by a waiting period T. As a function of T, we observe population transfer fringes with frequency equal to the detuning of the microwave frequency from the qubit transition frequency. However, if we turn on the high-power Raman laser during this time, we shift the energy level spacing, effectively changing the detuning. Putting the two curves side-by-side as shown in 4.1, we observe that stark-shifting the Ramsey profile during the wait time will cause the signal at T' to increase or decrease, as the intensity of the light at the ion changes. The value of the detuning here is important, because we would like for the stark shift signal to vary slowly enough that we stay within one rising or falling edge of the sinusoid for a while before needing to re-position at a new time T". Generally we choose somewhere around the 3rd or 4th edge of the fringe, in order to enhance our sensitivity. We also do not want the detuning to be so large as to drastically reduce our contrast, as the Ramsey fringe contrast goes as $\Omega^2/\hat{\Omega}^2$ where $\hat{\Omega} = \sqrt{\Omega^2 + \Delta^2}$ is the generalized Rabi rate. For the microwave addressing, $\Omega \approx 33$kHz. In terms of where to park the microwave for this stage, it is helpful to park the microwave "in the way" of the more aligned Stark shift beam. This is because you want your "better alignment" signal to correspond to lower frequencies (the difference between 1KHz and 2KHz is clearer than that between 11KHz and 12KHz). A reasonable choice of microwave detuning might be 5 kHz, and the shifts in frequency from the Stark shift were less than 200Hz.
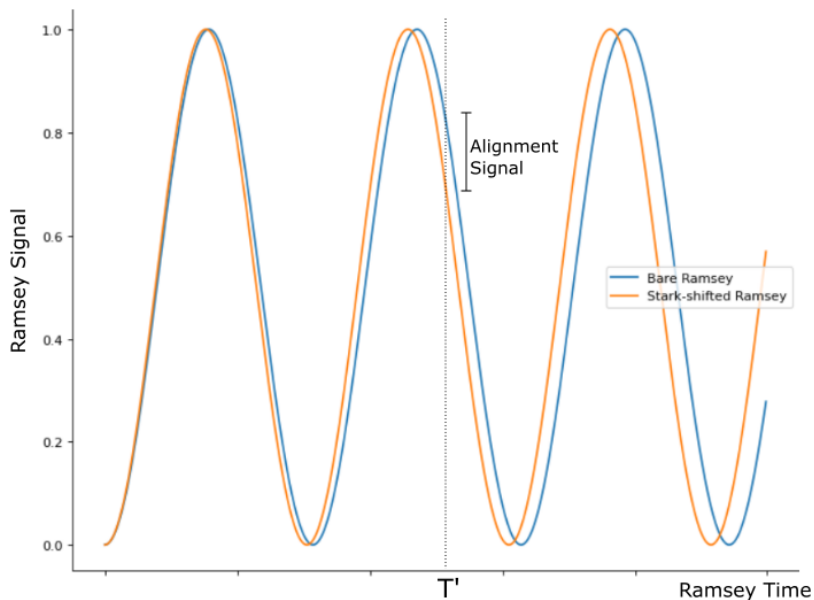
Figure 4.1: Example of alignment using Ramsey fringe shifts from the AC Stark shift. Note: in experiment the magnitude and direction of the stark shift (positive or negative differential) depends greatly on the polarization of the light, and in our experiment we utilize the 4th order Stark shift since the 2nd order differential Stark shift is small.

After repeated iteration of stepping the alignment stage along the axes perpendicular to the beam by a few microns at a time, and re-selecting a new Ramsey time whenever a rising or falling edge meets a peak or a trough, we can find an alignment that optimizes our Ramsey period. In order to obtain the optimum position along the beam axis, we do some book-keeping on the 2d optimization from before, shifting along the optical axis and looking for where the shift in the Ramsey period from the 2D translation is greatest (corresponding to the focus being the point of tightest beam).

This process was very fluid. I was changing the microwave detuning, the park time, and the alignment somewhat on the fly (while book-keeping as above for the alignment of the focus knob), but the better gauge for alignment is really the two photon Raman transitions, described next. This was just a necessary preliminary step.

27

4.2 Raman Transitions
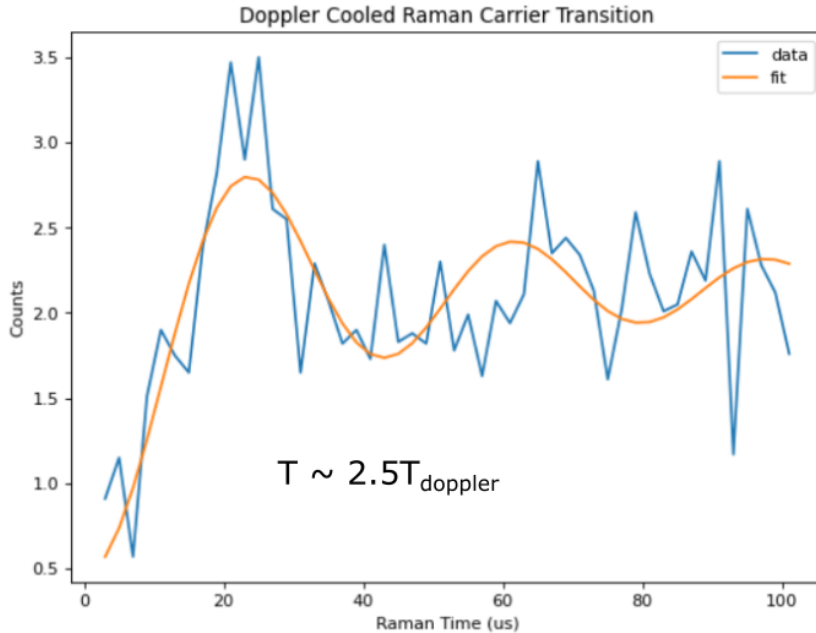
Figure 4.2: Raman carrier transition after alignment using Doppler cooling. The Doppler limit temperature $T_{Doppler}$ is approximately 480uK. For details on thermometry, see section 4.3

Once the alignment has been completed along both axes, after the beams are overlapped, the beat note stabilization circuit is engaged, and after checking polarizations of the beams are properly applied, we are able to see some Rabi signature. By 'proper polarizations' I mean that we use the lin-perp-lin configuration, wherein both beams are linearly polarized perpendicular to the B-field. This guarantees that the beams have balanced σ_+ and σ_- polarizations and induce the least amount of Stark shift. While we used Stark shift for alignment, we do not in general want it present in our Raman setup. At this point, the path length matching is used to optimize whatever coherent effect we see by increasing the overlap of the pulses. An example of the fluorescence signal from one carrier Rabi transition is shown in fig. 4.2. To finish our alignment, we tweak the final lens positions to maximize the Rabi rate. We also perform micromotion minimization by tweaking the DC voltages on the rods to maximize the Rabi rate as well. This helps because it makes the ion's motion smaller, so rather than sampling a large portion of the beam, it only samples

28

the small area where it is peak magnitude. However, we still have a hard time observing multiple full flops. While it is possible that this could still be some micromotion heating (we don't have perfect resolution on the DC voltages for perfect compensation), or some other unexpected mode participation, a significant portion of this 'decay' is some intrinsic loss of contrast from the ion's temperature, as I will discuss later.

4.2.1 Raman Spectrum

If we proceed to shift one of the AOM frequencies, this is equivalent to shifting the detuning of the overall transition. In this way, I obtained a full spectrum of the ion, shown in 4.3. The multiple peaks visible in the spectrum correspond to the Carrier transition, which flips the spin without coupling to motion, and multiple different types of sidebands which couple to motion in some way. Calculations using our trap parameters give that our secular frequency should be around 1.2MHz away from the carrier, so this allows us to identify our first order sideband transitions coupling to the phonon state of the harmonic oscillator. Because the frequency being shifted in this spectrum is that of the 215MHz path, we can see that an increase in the frequency on this AOM corresponds to an increase in the overall beat note between the two paths, so the peak at 216.2MHz is the blue sideband. The stability of the spectrum is evidence that the beat note stabilization circuit is working. When the beat note lock is not engaged, these spectra peaks would still exist, but would drift over time as described in Ch 3.

I am uncertain what the other peaks are, as they do not correspond to our axial trap frequency (which we estimate is ~200KHz) or our micromotion frequency (~20MHz). It is possible that the lower of the two peaks is a second order axial sideband. It is also possible that these are some kind of "switch" mode, where a phonon is lost from the trap along one axis but gained along another, but the frequencies of these peaks don't align particularly well to the differences in the other mode frequencies. This is still a topic of exploration for when our Raman system is started up again.
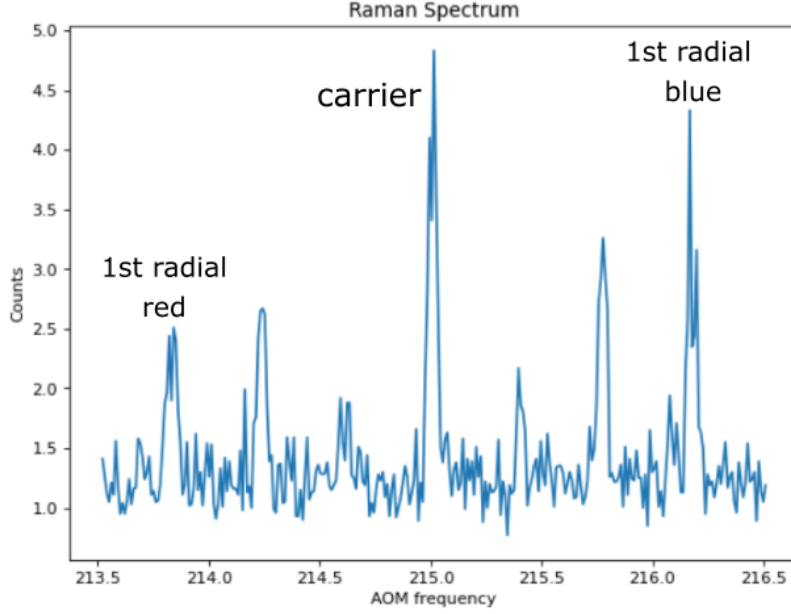
Figure 4.3: Raman spectrum obtained from sweeping AOM frequency after RSBC

4.2.2 Thermal requirements

While Doppler cooling is sufficient to keep the ion relatively cold in its kinetic energy, the required Temperature for our ions, determined by the Lamb-Dicke regime described in Ch. 2, is below the level that even a theoretically perfect Doppler cooling setup could produce. Considering a photon spontaneously emitted from the 20MHz linewidth $\left|^2P_{1/2}\right\rangle$ state during Doppler cooling, the uncertainty in the photon's frequency corresponds to a distribution of momentum kicks on the ion. This is equivalent to a temperature we call $\mathrm{T}_{doppler} = \frac{\hbar\gamma}{2k_b}$, which for this transition is 480 μK. The motion of the ion will be described now in terms of its phonon state in the 1.2MHz harmonic oscillator, the energy levels of which are equally spaced by 1.2MHz. Assuming that the motion of the ion follows a Maxwell-Boltzmann distribution, each phonon state will have different occupation probability according to the temperature

$$P_n(T) = \frac{e^{-E_n/k_bT}}{Z(T)} \tag{4.1}$$

where $Z(T) = \sum_n e^{-E_n/k_bT}$. I extract an average phonon state, $\bar{n} = \sum_n nP_n$, converting a temperature to an average phonon occupation, and vice versa. Even for an ion at

30

the Doppler cooling limit, the average phonon occupation number is around $\bar{n} = 7.4$. Again, the required temperature for the eventual implementation of the Molmer-Søresnson interaction is given by the Lamb-Dicke regime, characterized by parameter $\eta = kx_0$. In the two-photon process we use, the wavenumber of the field k generalizes to $|\Delta\mathbf{k}|$, the difference in wavevectors of the two beams. Plugging in these values for our experimental parameters and geometry gives $\eta = 0.2$ as an estimate for the Lamb-Dicke factor. We will be in the Lamb-Dicke regime when $\eta^2(2\bar{n} + 1) \ll 1$. This implies that our average phonon occupation number must be $\bar{n} \ll 12$, so our target $\bar{n}$ is around a single phonon or less. After theoretically perfect Doppler cooling with $\bar{n} = 7.4$, we are still too hot, so another method of cooling is required.

4.2.3   Sideband Cooling
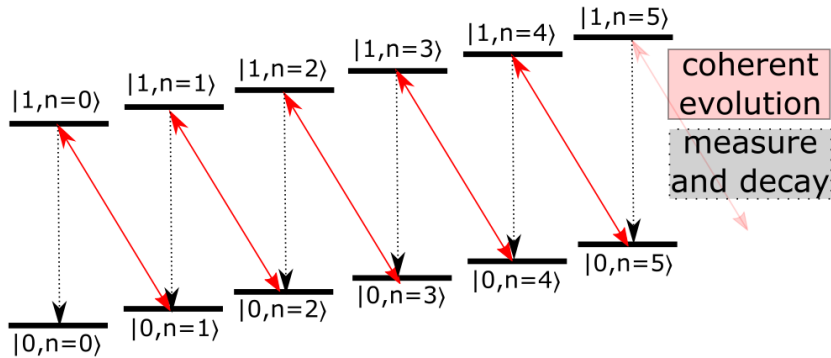
Figure 4.4: Continuous Raman sideband cooling

Raman sideband cooling is the method by which I was able to coherently reduce the phonon number in the system below the limits of Doppler cooling. Using the red sideband transition I found in the spectra, I park at its frequency while simultaneously applying a weak optical pumping light. What does this do? As seen in fig 4.4, the red sideband transition removes a phonon in order to flip the state of the ion to the bright state. The optical pumping light takes the bright state ion and drops it to the down-state. The only phonon state which cannot participate in this process is the ground state, as it doesn't have a red sideband transition. In this manner, we can sweep the population from higher phonon states down into the ground state. Why does the optical pumping light have to be weak? If the pumping light is too strong, we run into a quantum Zeno effect, where the ions are

measured by the light so frequently that they do not have time to coherently evolve along the red sideband. This is continuous Raman sideband cooling. Another method known as pulsed sideband cooling exists, where the red sideband and optical pumping light are switched back and forth at optimized intervals. This avoids the issue of the quantum Zeno effect, but the efficiency is not much greater overall, and this requires more overhead in terms of pulse sequence control and timing. Unfortunately, the efficiency of the sideband cooling technique is not uniform for all phonon states, and actually experiences near-zero efficiency at around $n = 112$ for $^{171}\text{Yb}^+$ [10]. For this reason, we also require a second order red sideband transition for our ion, which does not experience a dip in efficiency at this phonon value [10]. Sideband cooling drastically improved the resolution of the transitions, representing their cooled state, which is measured next.

4.3   Thermometry

One point of note is that the carrier transitions and sideband transitions do not occur at the same rate, but rather vary according to the phonon state of the ion. The Debye-Waller factor $D_{m,n}$ characterizes this difference, where $\Omega = \Omega_0 D_{m,n}$ with

$$D_{m,n} = e^{-\eta^2/2}\eta^{n-m}\sqrt{\frac{m!}{n!}}L_m^{n-m}(\eta^2) \tag{4.2}$$

such that n and m are the initial and final phonon states (with n being the larger of the two, regardless of which was initial or final), Ω_0 is the ground state carrier Rabi frequency, and $L_m^{n-m}(\eta^2)$ is the generalized Laguerre polynomial [11]. In the Lamb-Dicke regime however, we can approximate the Debye-Waller factor as only being composed of its lowest order terms. While the carrier remains relatively unaffected, the sideband transitions have a noticeable shift in their rate and can be measured.

$$\Omega_{carrier} \approx \Omega_0(1 - (n + 1/2)\eta^2) \tag{4.3}$$
$$\Omega_{RSB} \approx \Omega_0\eta\sqrt{n} \tag{4.4}$$
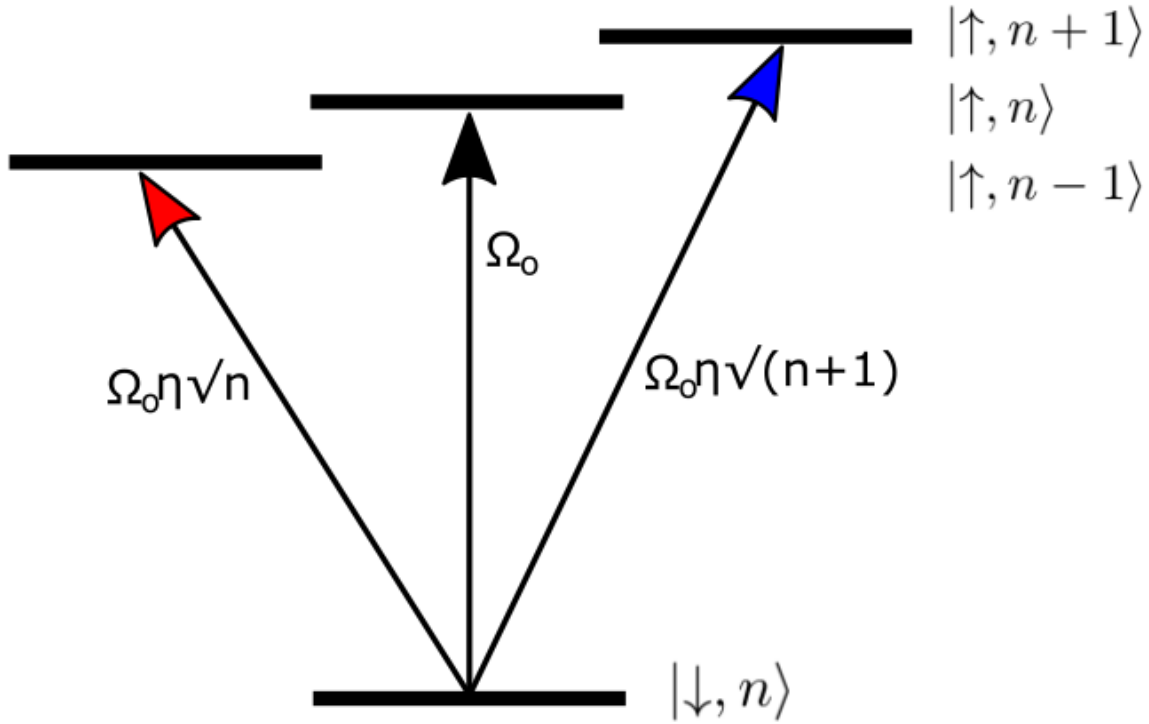$$\Omega_{BSB} \approx \Omega_0\eta\sqrt{n+1} \tag{4.5}$$

Figure 4.5: Different phonon states undergo Raman transitions

4.3.1 Fitting to thermal distribution

I sought to us this as as a method for thermometry. My goal was to create a function which could be fit to our experimental data to extract the temperature. After Doppler cooling, the ion is in some mixed state governed by a distribution determined by its temperature. The idea is that when a transition is driven, each of the phonon states contribute a different frequency, and the amplitude of that frequency is given by the relative population of that state in the distribution. The strange features in 4.2 could be interference between many different phonon states with slightly different frequencies. Much like a Fourier decomposition, I could extract the frequency components from our signal to find the original distribution, and extract a temperature. When I first attempted this, it failed because I had not considered the fact that the basis vectors were not orthogonal, which is to say that the frequencies of adjacent phonon states were too similar to simply find a projection to subtract away and work on the residual. It is also worth noting that I didn't know

precisely what the frequencies for the various phonon modes were, since our estimation of the Lamb-Dicke parameter could be incorrect up to some geometric factors. The one assumption I could make was about the shape of the distribution, because we could assume that with Doppler cooling, the ion should be in some thermal state. To address this, I added in the assumption that the phonon state populations fall into a distribution with some form parameterized by their temperature. The initial choice was to use the Maxwell-Boltzmann distribution, although I included the option to simulate other parameterized phonon state distributions. This time, I started by working forwards, starting at a temperature to obtain a phonon state distribution. Using the theoretical value of η as a guess, I incoherently summed the expected transition signal from each phonon state according to their probabilities given by the thermal distribution. You can see examples of the Raman transition curves I simulated in the figures below.
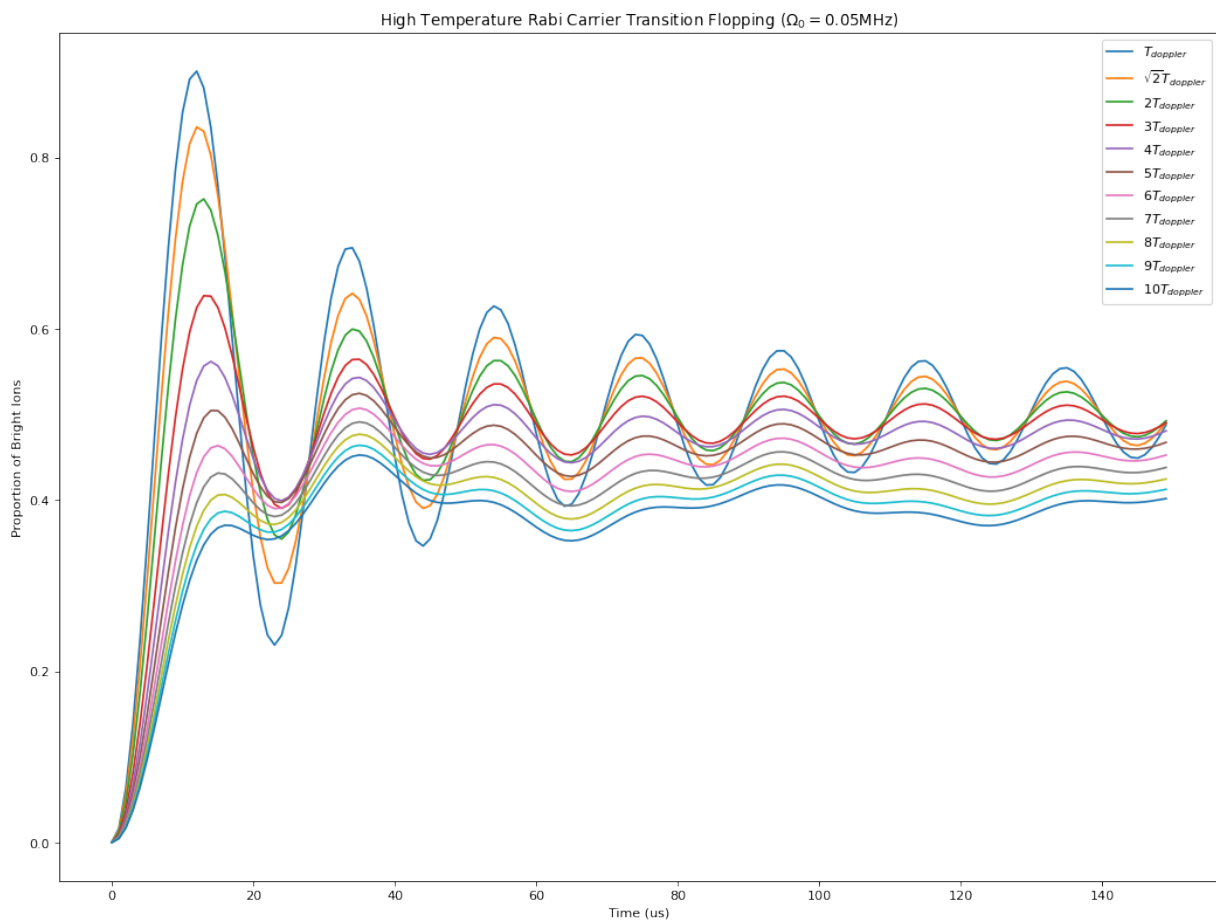
Figure 4.6: High temperature Carrier transition simulation
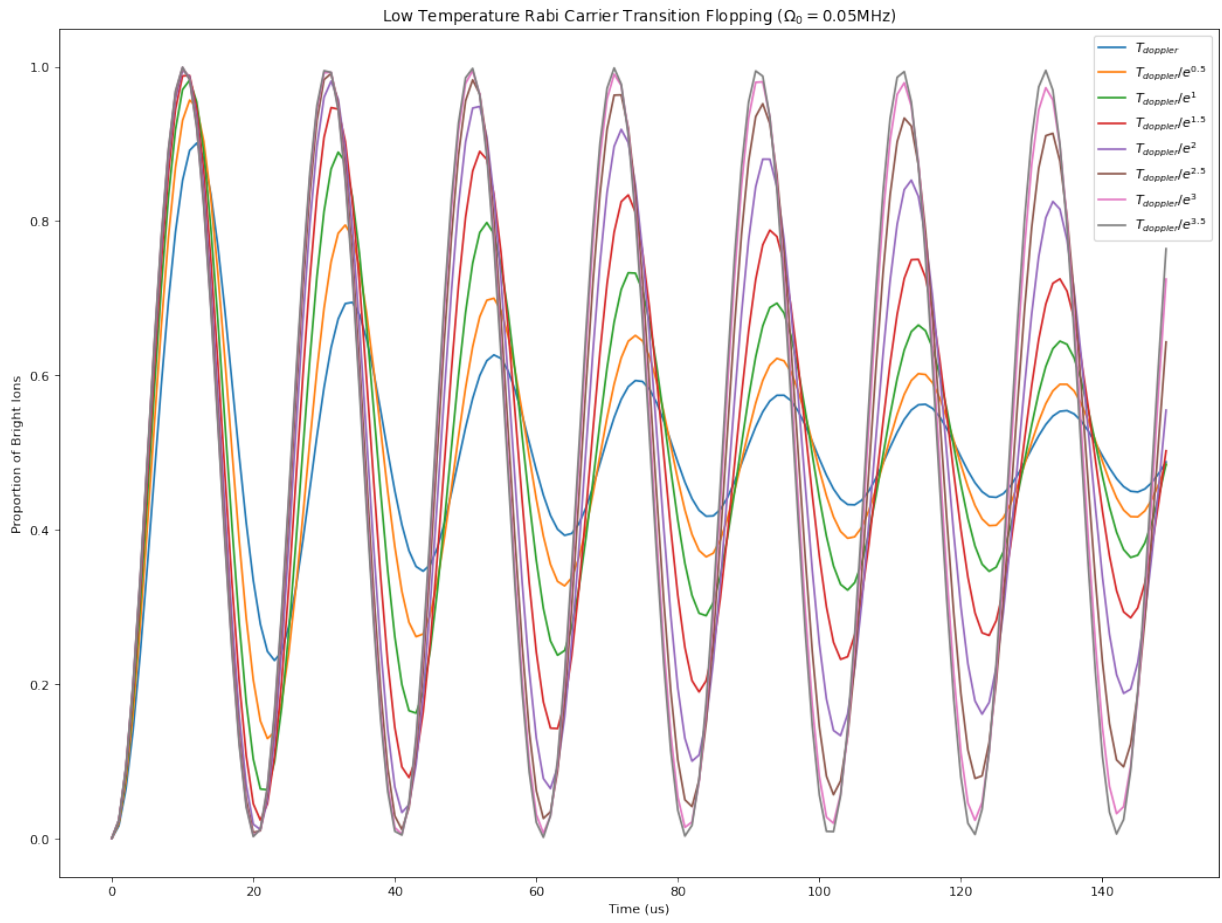
Figure 4.7: Low temperature Carrier transition simulation
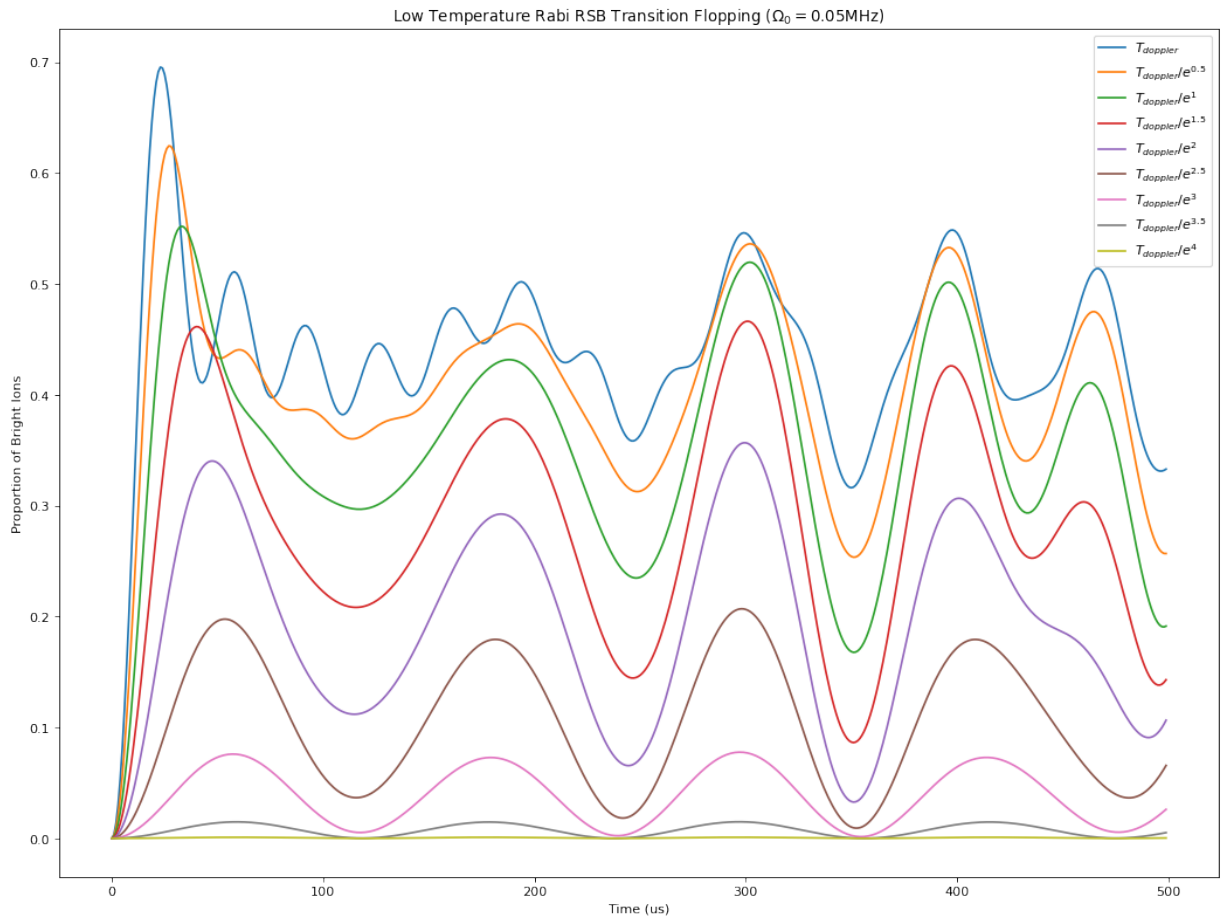
Figure 4.8: Low temperature red sideband transition simulation
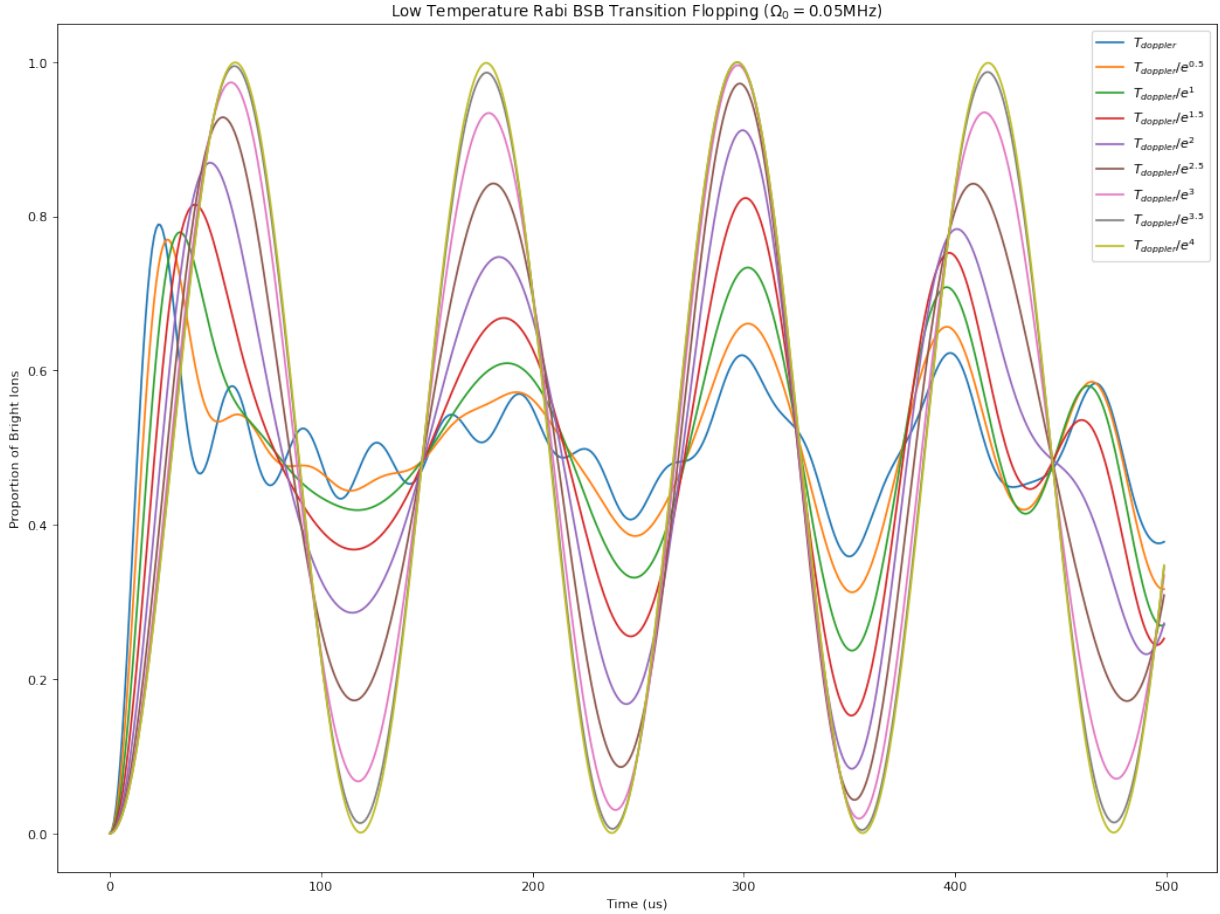
Figure 4.9: Low temperature blue sideband transition simulation

The simulations do demonstrate a "decoherence" of the signal, although it should be stressed that this is still coherent evolution, just of an ion in an initially mixed state. It is easy to notice that as the temperature gets lower, the states approach pure sinusoids, representing that only the ground state contains significant population. For fitting to experimental data, I would provide an approximate guess, and then feed the distribution and the data to a curve matching algorithm in Python. The curve fitting does work, although for higher temperatures and for noisy data the fitting obviously becomes more dodgy. Fortunately, though, the carrier transition's flopping as a function of temperature is actually more sensitive around the doppler limit than for post-SBC temperatures, so this method was what I used for the data in fig 4.2, obtaining a temperature of $2.5\text{T}_{doppler}$=1.2mK, or $\bar{n} = 18.5$. This is well above the Lamb-Dicke limit of $\bar{n} \ll 12$. On the other hand, the

38

sideband cooled results presented below show far improved temperatures.

These sideband-cooled experiments all utilize a 30 ms continuous sideband cooling step immediately after the Doppler cooling. In fig 4.10, I have plotted the sideband cooled carrier transition, which gives us an accurate guess for the ground state carrier Rabi rate for use in the fitting for the sidebands. We find this Rabi rate $\Omega_0 = 30$ kHz. It is difficult to trust the low-temperature carrier as a thermal sensor though, since the carrier transitions for all low phonon states should be very close.
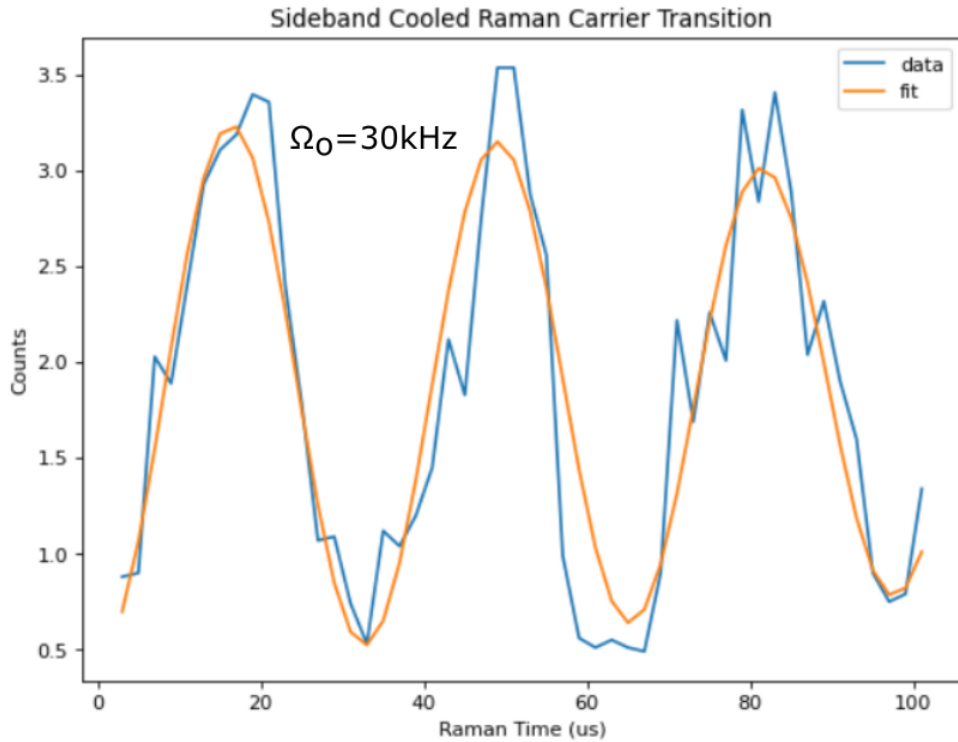
Figure 4.10: Sideband cooled carrier transition

4.11 shows the blue sideband flopping, which now allows us to accurately extract the temperature as T= $0.11\mathrm{T}_{Doppler}$=53μK. Unfortunately, the fitting for the Lamb-Dicke parameter was not working particularly well, so the uncertainty is still quite high, ranging from 0.17 to 0.3, although fittings all throughout this range agree on the value of the temperature. Plugging back into the thermal distribution gives an expected phonon number for an ion at this post-SBC temperature of $\bar{n} \approx 0.39$. At this temperature, roughly 3/4 of the ions after the sideband cooling sequence are in the ground state. This is well below

the Lamb-Dicke limit, and represents roughly a 50x reduction in the phonon state from Doppler cooling to CSBC.
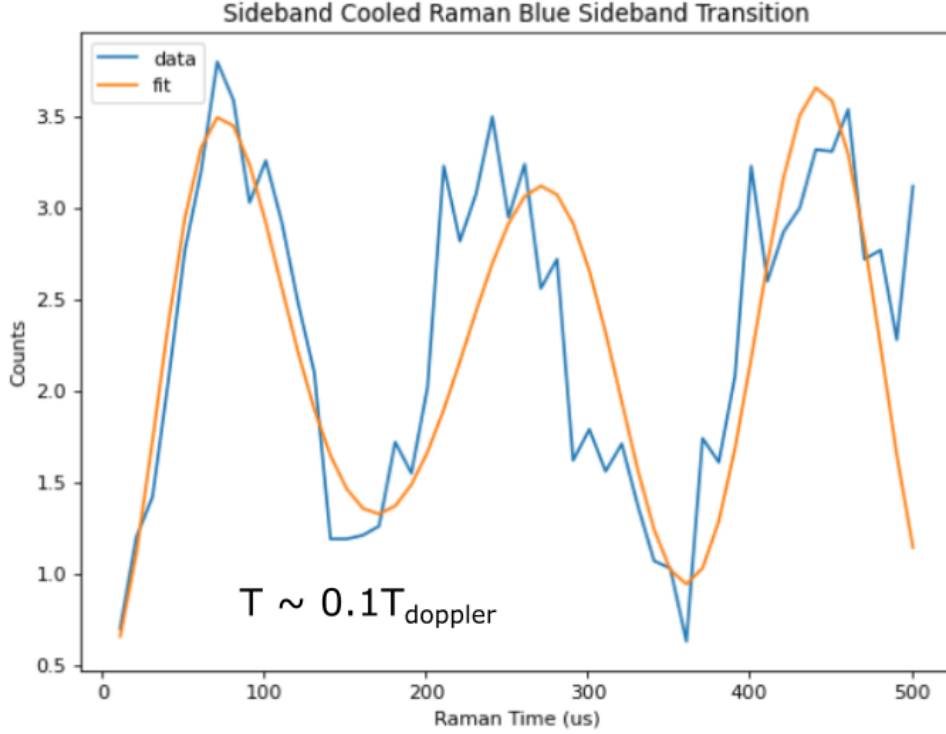
Figure 4.11: Sideband cooled blue sideband transition

As seen in 4.12, the red sideband flopping is much less amenable to this technique. During alignment, we observed a signal very similar to this when micromotion was particularly bad. It is also possible that this is some other decoherence channel we have not yet described, or perhaps related to the unknown peaks in the spectrum. Regardless, if we consider this signal to be some background decoherence mechanism, then the fact that we don't observe much of anything is actually expected for a very cold RSB transition time scan, since the ground state doesn't have a phonon to trade away to flip its qubit state. If we did observe a signal, it would be weak, and at the same frequency as the sideband cooled Blue transition. This is because for low temperatures, $\Omega_{BSB} \approx \eta\Omega_0\sqrt{n+1}$ and $\Omega_{RSB} \approx \eta\Omega_0\sqrt{n}$. We can see now that n=1 for the red sideband and $n = 0$ for the blue sideband will flop at equal rates, and because there is no $n = 0$ red sideband transition, the most dominant phonon state would be $n = 1$. If we wanted to verify this equivalency,

40

we could first apply a $\pi/2$ rotation about the Bloch sphere, putting the sideband cooled ion into the bright state of $n = 0$, and measuring a flopping signal down. The ion signals would then be roughly shifted to $n + 1$ flopping, but inverted since the ion would be starting in the bright state. I could perform thermometry on this distribution, but because the carrier frequency is slightly different for each phonon state, any errors of imperfect carrier $\pi/2$ flopping would result in each original phonon state's flopping being split between n and $n + 1$ flopping with a ratio dependent on n. There would also in principle be no $n = 0$ population. While possible, the thermometry would be riding on the back of some assumptions on the form of the distribution, which are less likely to be accurate after the rotation. Overall, the goal of looking at the red sideband flopping was to confirm that there was no signal, indicating that the ions were primarily in the ground state. We did find that there was no signal for the frequencies we expect, but the other decohered signal we observe can hopefully point us towards improvements in our method. Regardless, I will next turn to an alternative method for thermometry to verify temperature for the system.
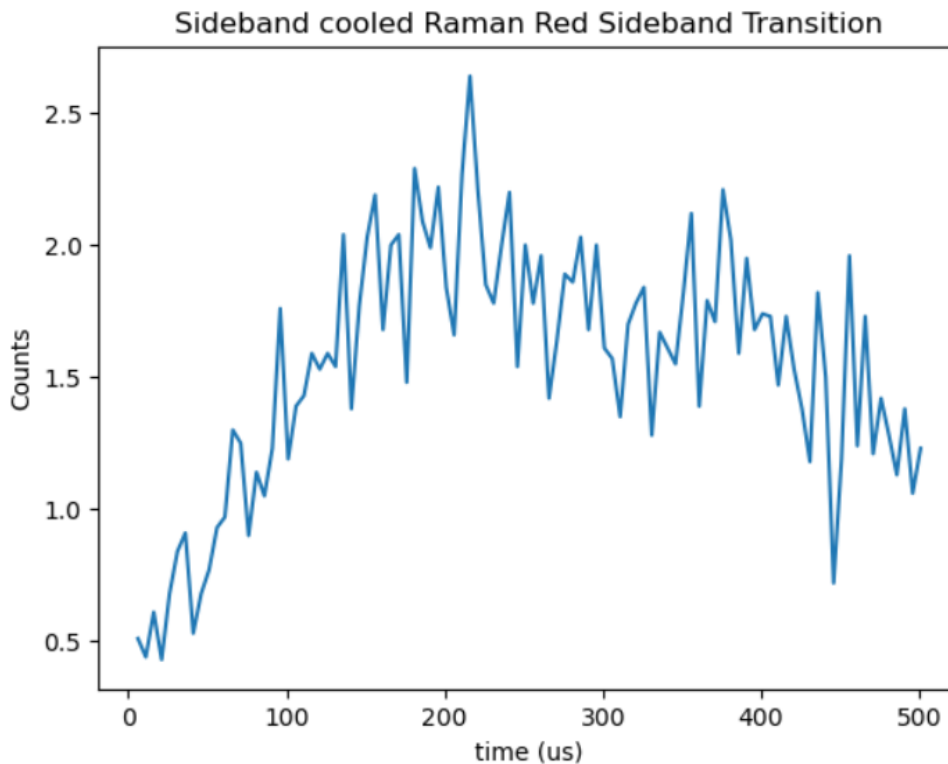
Figure 4.12: Sideband cooled red sideband transition. This was starting with the ion in the dark state, for which we expect no red sideband transition to occur for n=0. We could have begun with a $\pi/2$ pulse to flip the state to bright, which would equate to shifting all few-phonon state flopping to inverted flopping of $n+1$, starting bright and flopping to dark. No fit is included here because the dominant Rabi frequency should be equal to that of the blue sideband, so the fitting will be highly inaccurate. However, the lack of signal here is a good indicator that we are in the low temperature regime.

4.3.2 Thermometry through sideband comparison

Another method of estimating the ion temperature is by comparing the relative strengths of the first order sidebands in the ion's spectrum.

$$P_{rsb}/P_{bsb} = \frac{\bar{n}}{1 + \bar{n}} \tag{4.6}$$

[9]. Using the sideband cooled spectrum in fig. 4.3, I estimate $\bar{n}$=0.6, which would correspond to a temperature of $0.13T_{Doppler}$.

42

4.4   Raman Results and Conclusions

I was able to bring up Raman transitions. The required Ramsey alignment using Stark shift, implementation of a beat note stabilization circuit and path length matching. I utilized the different Rabi rates of the phonon states to simulate measured fluorescence for different thermal distributions of the ion's motion. I used this form as a basis for a fitting function to estimate the temperature of an ion from experimental data. I implemented a Raman sideband cooling sequence, and measured a significant improvement in the thermal state of the ion. Even in the worse case of two thermometry measurements (fitting the flops to a thermal distribution and using relative sideband strength) of $\bar{n} = 0.6$, and even assuming the largest Lamb-Dicke parameter from the simulations of $\eta = 0.3$, we would still evaluate our status with respect to the Lamb-Dicke limit as $(0.3)^2(2(0.6) + 1) = 0.2 \ll 1$. When using only Doppler cooling, with a fitted temperature of $2.5\mathrm{T}_{Doppler}$ in the best case scenario for the Lamb-Dicke parameter, we have $(0.17)^2(2(18) + 1) = 1.06 > 1$. There are a few outstanding points to be made. Firstly, the post-SBC phonon distributions may not actually follow a Maxwell-Boltzmann distribution, but rather some other form of distribution that represents the competition of micromotion and sideband cooling. Other forms of distributions can be tested in the future, though the assumption of a this form does not seem unreasonable. Furthermore, there is still some remaining uncertainty about curious peaks in the ion's spectrum which I was not able to probe before the Raman system went into experimental hibernation.

In conclusion, I have utilized the method of Raman sideband cooling to cool our ions near the motional ground state. While we do not have a definitive answer on what our Lamb-Dicke parameter is exactly, even conservative estimates put us within the Lamb-Dicke regime, where we can expect sufficient decoupling of our motional and qubit states for the implementation of our entangling operation.

Chapter 5

Blade Alignment
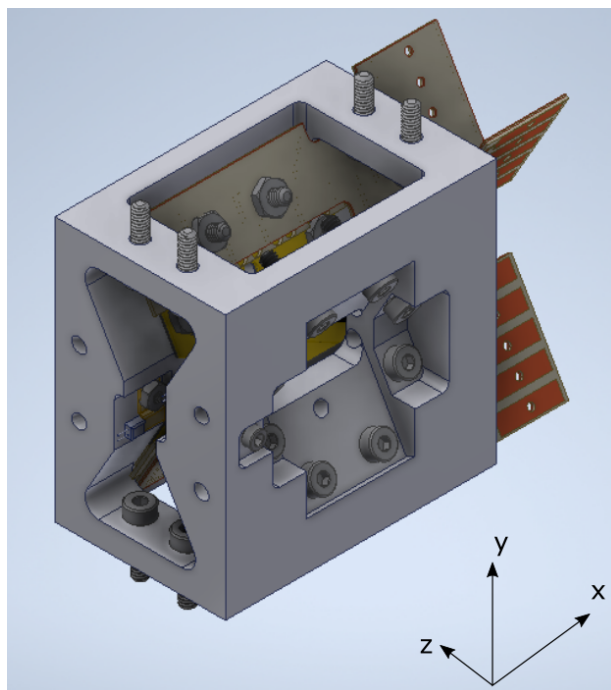
Figure 5.1: The blade holder CAD model with internals attached

In this chapter, I will transition from discussing the work on the four-rod trap system to the future apparatus our group has been working on. This apparatus, the blade trap, replaces

the four cylindrical electrodes with four thin blade-like electrodes split into five segments each. I will lay out the reasons for this change, the complications that arise with regards to alignment, the required alignment tolerance, the strategies and tools I developed, and my progress in performing an alignment procedure. I will be using the names that I and my lab mates have assigned to the various components, which are labelled in fig 5.3.
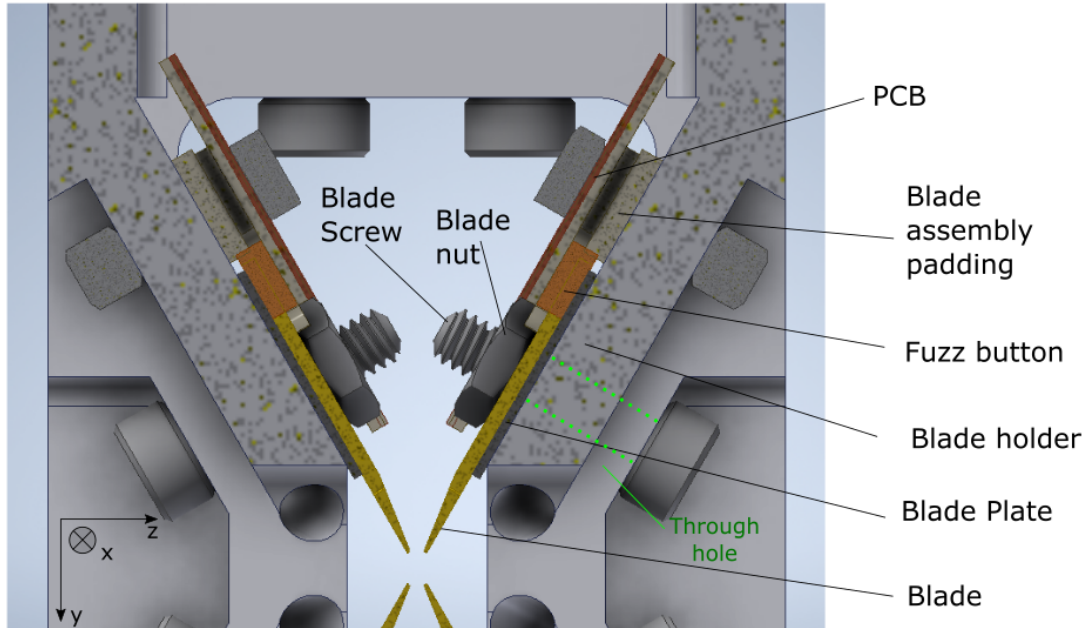
Figure 5.2: Cross-sectional view of the blade and other internals

Regrettably, the nature of the experimental work done in this chapter is primarily comprised of small iterative changes in alignment techniques and strategies performed on the same units. Not only would photos look very similar to each other, but also the amount of manual dexterity required to work on this project left it terribly difficult to take photos mid-action. To compensate for this, I will illustrate using CAD models when necessary. Easier photo capturing will be enabled by the setup I work towards at the end of this chapter.

5.1 Four rod trap to Blade trap

The bulk of the trapping physics remains the same in a blade trap system as compared to a four rod trap system. In this new configuration, each rod is divided into five segments each with independent control, depicted in fig 5.3. The segmentation of the rods into 5 segments each allows for a greater control over the trap strength along an ion chain. For example, if the amplitude of the outer segment RF is greater than the center segment RF, then a higher frequency pseudo-potential is generated for the outer regions. This is significant since it can allow us to more effectively control the ion spacing and the shape of the motional mode profiles, which might be desirable for individual addressing procedures or Hamiltonian engineering. Additionally, the reduction of the distance from the ion to the electrode R_0 creates a higher overall trap frequency. This is desired since higher trap frequencies correspond to faster gate times [12]. All of these reasons have yet to take into account the improved design of the new system, which improves the detection and Raman NA from 0.2 to 0.5. In addition, the vacuum level of the new system is estimated to improve upon the old system by an order of magnitude in pressure, reducing background collisions and thereby improving ion lifetimes.
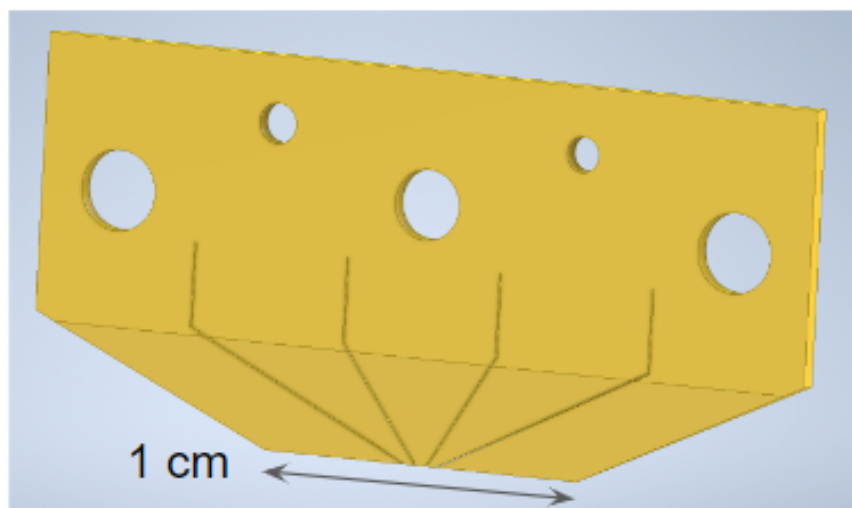

Figure 5.3: Rod broken up into a 5-electrode blade

However, with these improvements come additional complications. With all of the custom design that went into this project, the actual alignment of the electrodes falls on our hands rather than a manufacturer. Misalignment of the blade electrodes can create

unexpected features in the potentials near the ion. In particular, it can result in misalignment between the DC null line and the RF null line, which is the 3d analogue of having stray electric fields pushing the charged particle away from the center of the trap. While a DC shift can re-center these axes on each other at one point to optimize a single ion, we have a much more difficult time re-aligning the null-lines for the entire chain - certain configurations may be impossible to properly compensate. As mentioned in chapter 2, in the four-rod trap picture, stray electric fields from the harmonic potential at the ion position result in micromotion sidebands, which can contribute to heating and can break our coherent entangling interactions. The same holds for the blade trap, although the micromotion can now be uncompensatable and highly anisotropic along the chain. Any one ion with high micromotion could heat up the entire chain, so the entire DC-null line must be aligned to the RF-null line to as accurate a degree as possible. My goal on this project is to reduce the micromotion from this misalignment as much as possible, in conjunction with developing a process for assembling the internals in our system. The ideal positions of the blade electrodes is shown in fig 5.4.
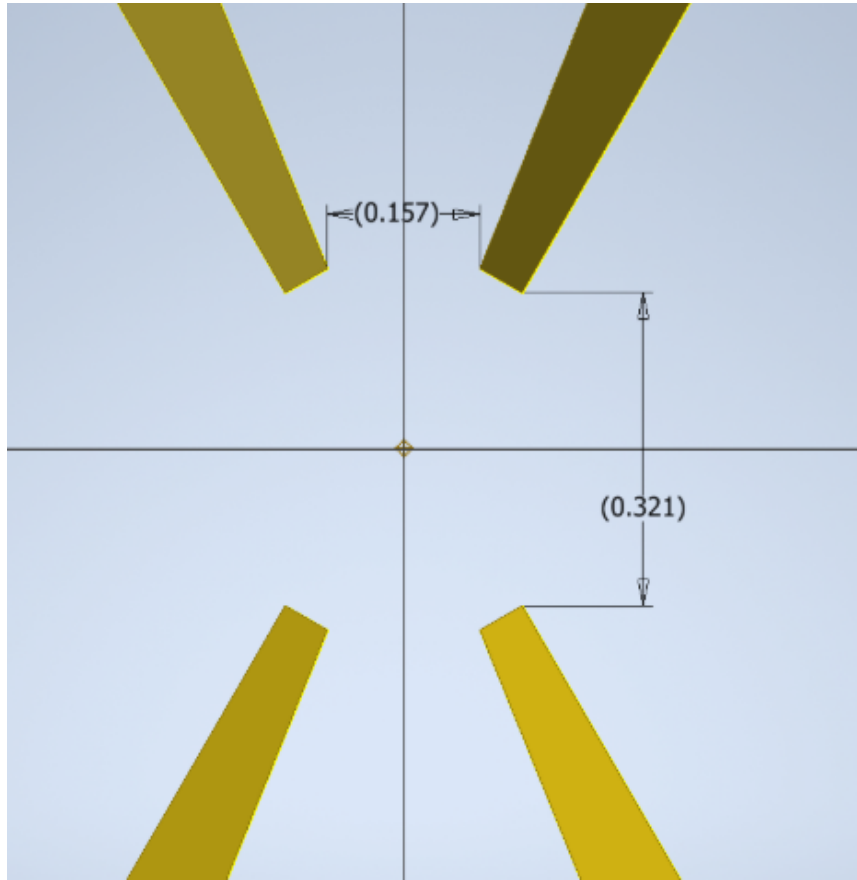
Figure 5.4: Ideal distances for blade alignment, cross section view. Units are mm. 157μm is the acute pair, 321μm is the obtuse pair.

5.2 Misalignments

The first step in addressing the challenge of blade alignment was to quantify how well I should aim to align the blades. I arrived at the target value of ±5um (along any given dimension) for a few reasons. Firstly, some of the errors we have very little control over, such as electrode corner feature errors and blade machining uncertainties are already on the order of multiple microns (shown in fig. 5.5). Therefore, even perfect nominal alignment below this level might not correspond to optimized alignment once the ions are being trapped. In addition, it was previously verified in work done in Dr. Crystal Senko's group that the most critical misalignments are those which are axially asymmetric. These mis-

alignments generally cannot be compensated along the whole chain by modulating the DC voltages, which is expected, since an axially symmetric misalignment could be approximated in the cross-section picture whereas axially asymmetric misalignments cannot. The determination of what is acceptable and unacceptable misalignment comes from simulations of ion trajectories in the resultant potentials, and a threshold is identified at the point where the kinetic energy from micromotion is at the level of 2mK, thus conflicting with Doppler cooling [1]. The three axially asymmetric misalignments are depicted in fig 5.6 with these threshold values. The translational misalignment should be below 5um, and the angular misalignment can be at most 0.1^o; the final axially asymmetric misalignment corresponds to tilts of the blade holder planes, which must be below 0.2^o [1]. The 0.1^o misalignment corresponds to a 18μm misalignment along the extent of the blade plane, which is tilted 60° from the vertical axis of the holder, meaning that along either imaging axis (the acute pair or the obtuse pair) one would still measure at least 10um displacement from the expected range. The tilt of the blade holder planes would yield a 30μm difference in the focus between the corners of opposite blade segments. While translation and angular misalignment can be handled with proper realignment, the blade holder plane tilt requires an additional step to adjust. It should be noted that the misalignment tolerances presented here are for the assumption of a single blade's misalignment, and in principle would be worse if such misalignments existed on each blade.

With the tolerances on blade production and the required values for micromotion minimization, I settled on a target of $\pm2.5\mu$m alignment, referenced at the outer blade segments. Because there isn't any datum to reference the absolute positions of the blades, this means that the measurements between acute and obtuse pairs should be within 5μm of target values, shown in fig 5.4. Another goal for the alignment procedure is to have as little physical contact with the blades as possible, as non-metals on the electrodes can introduce RF heating or burn. Finally, the alignment process should take as little time as possible, ideally an hour or less. Increased time of exposure corresponds to increased likelihood of dust or oils contaminating the sample. Finally, all procedures and tools must be clean-room compatible since our final target vacuum system is XHV-level.
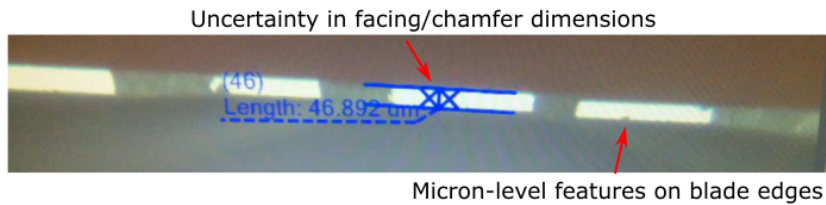
Figure 5.5: Corner features and machining tolerances on the blade dimensions on the order of 1-2 um
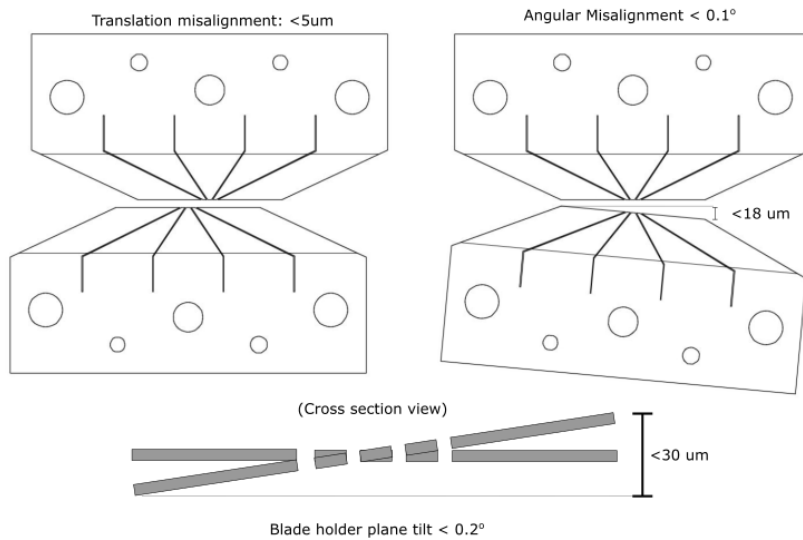
Figure 5.6: Representation of the three critical misalignments in terms of excess micromotion. The other, axially symmetric misalignments can be compensated for using DC voltages. Misalignments not drawn to scale

5.3 Alignment Methods

Before addressing this challenge with physical alignment, a few design steps were taken. The blade holder is a monolithic piece of Shapal, a proprietary material composed primarily of Aluminum Nitride doped with Boron. It maintains most of the high thermal conductivity of the Aluminum Nitride, while gaining machinability due to its softer composition. However, even with Shapal being easier to machine, we still were only able to

have the tolerance on the dimensions for blade alignment at or above the 1 thou level, $\approx$ 25um. To accomodate this, we have opened the through-hole for the blade screw to allow for more range of motion, approximately 100um from the central point, which should allow accurate alignment even with the loose specs. To address the possibility that the vertical dimension (normal to the blade plane) might be too far away for the blades to properly align, I worked with another student to acquire blade plates of varying thicknesses to make up for the displacement from the blade holder. With these first steps in mind, I will now describe the physical alignment using the setup.

One of the first lessons I learned in this process was the importance of seemingly unimportant decisions. For example, when I was first practicing alignment, I was aligning one blade to the approximate visual center, then placing the next blade and repeating. This not only required many iterations of re-alignments, by virtue of my initial blade position being a complete guess, but also just the act of inserting a blade into position once the others were aligned made blade-on-blade contact far more likely, if not inevitable. From this, I adapted to placing all of the blades into the holder at the outset, in the "retracted position" (as far away from the trap center as possible) and tightening them there. In this retracted position, the risk of blade-blade contact is reduced, so all blades can be safely attached to the system before alignment commences. The second half of this initial lesson was that I required one of the blades to align to the blade holder itself in order to be close enough to the center as an initial guess. Otherwise, I would be performing too many re-alignments, since my figure of merit for alignment is the position of the blades relative to each other. This first 'referenced' blade would then allow me to get all other blades into position fairly close to the optimum position. For this first blade alignment, I determined that the best feature on the blade holder for referencing purposes was the PCB mounting through holes. While they also had similar tolerance issues to the blade screw through holes, they should be fairly well-toleranced in their distances to each other and to the other through holes on that plane. I determined that the best measures for this was to measure the circle to circle distance in an X pattern, between the blade alignment holes and the PCB mounting holes, as shown in fig 5.7. Unfortunately, these two circles are out of focus, and the required imaging plane for both of these holes is not normal to the surface, so an extra tilt and a slight geometrical re calibration was required in order to correctly identify the projection of this distance onto the optical plane of the camera used during this step, and also to machine a custom angled block to hold it at that tilt.
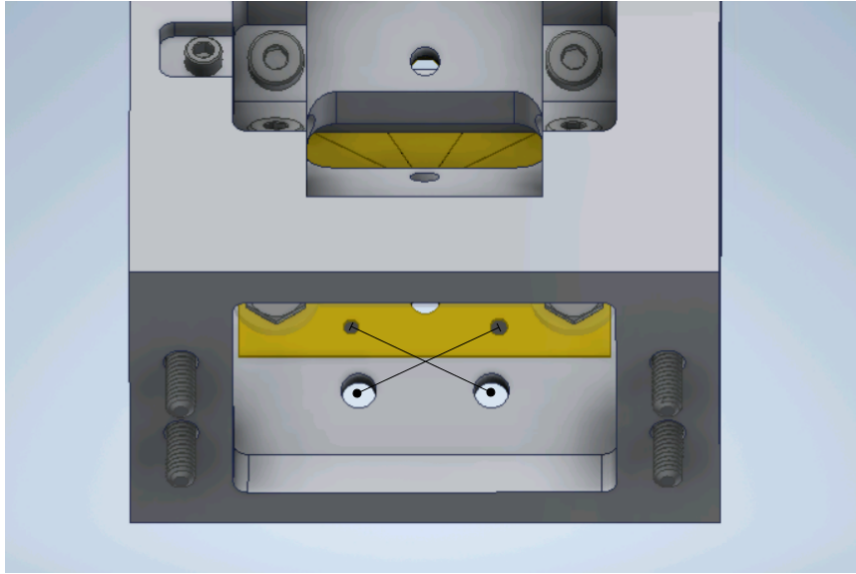
Figure 5.7: A visual representation of the measurements used for aligning the first blade to the blade holder.

In the end, this step isn't perfect, but it creates a good enough first position to align the other blades. With this step in place, the alignment of the other blades to this first blade would create 'initial alignment,' which could then be tweaked during 'fine alignment' until the blade positions were completely optimized and within the target values.

Another critical issue arose when I was performing this fine alignment. Originally, my plan was to use the alignment holes on the blade itself to make 2-point contact using tweezers and translate the blade by pushing and pulling the tweezers to manipulate the blade. After many attempts, this method of alignment proved to be simply too chaotic. One primary reason for the failure is that this method of alignment only allows controlled movement in a single direction. The tip of the tweezers are quite small compared to the maneuvering hole, which meant that only one side could be pressured at a time. With the force only working in one direction, there was very low stability, and the blade would move in the direction of the force by an uncontrollable amount. Fine motion was nearly impossible. In addition, the use of tweezers to apply force put the blades at greater risk of scratches or breaks, and the dexterity requirement on the manipulation of the tweezers added a After this discovery, I considered using a suction tool, which would give stability to the forwards backwards alignment. In testing, the suction was very weak, and furthermore, the material of the suction head would be a contaminant for the final vacuum. I went back to my initial alignment strategy, in which I used just a gloved finger to move the blades into

a retracted position where they were all stable on the blade holder but far away from the alignment position. After trying out a few different techniques, I found that I was able to successfully move the blade with fine control using my gloved finger. The key is to maintain pressure with your finger on the blade while pressing up on the screw head underneath to ensure that the nut has as little friction as possible. This is best performed on the bottom side by an Allen key, so that as soon as the blade is in position, it can be tightened down. While using a gloved hand still introduces contaminants, the contaminants are far away from the blade tips near the ions, so any imperfections in the blade heating there will not be as bad. The stability gained by using my finger allows for iterative alignment steps between the two sides without having to worry about overshooting.

I found that the tightness of the nut after initial alignment is crucial to the maneuverability of the blade during the fine alignment. If the nut is too tight, the blade will seem to slide back and forth but return to approximately the same position. This is because the friction between the blade and the blade plate is less than the other frictions in the system (nut-blade, blade plate - blade holder, or screw - blade holder). The blade will simply move with respect to the blade plate, maintaining contact with the nut and causing the nut to bend a few microns and misalign from the through-hole's axis. Once the pressure is removed, the blade will slide back along the blade plate to the original position. In order to successfully complete a re-alignment, the blade needs to translate with respect to the nut. This can be done in two different ways. First, I can "walk" the nut and bolt, where I allow the nut to flex in its through hole in the above manner, then push it in the other direction with a tweezer tip to release the corner contact. A crude drawing of this process can be seen in fig. 5.8. As the blade is pressed forward to the center of the trap, the forward edge of the nut will make stronger contact on the blade than the back edge of the nut, and the similar process occurs for the screw head on the holder. By pulling the screw in the opposite direction, I disengaged this contact point, redefining the position of the nut to the blade.
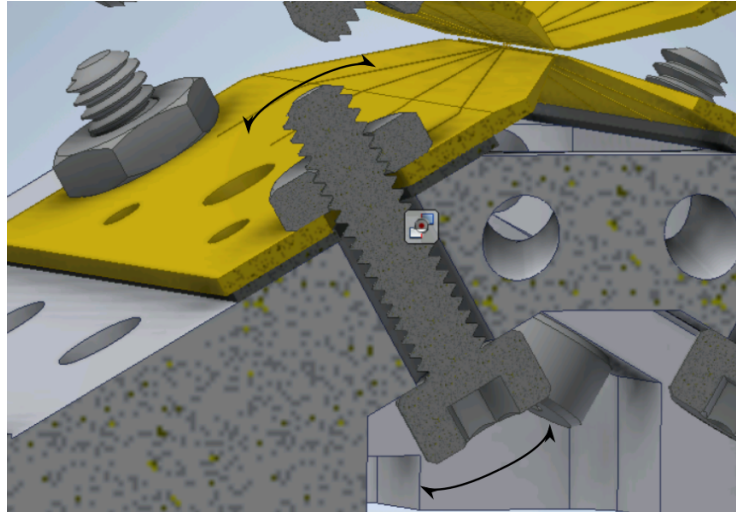
Figure 5.8: "Walking" of the nut and bolt for allowing blade motion

This method can still lead to some scratching, and also has similar tightening problems afterwards, where the new position after tightening is difficult to control. For these reasons I decided to avoid this method moving forward. The second and preferred method is to have the nut sitting on the screw just above the blade, making as little contact as possible with the blade. Because everything here is through, this means that a constant upward force must be applied to the screw head to lift the nut off the blade. Once the blade is in position, the nut is tightened. This method minimizes scratching and has better control over the final blade position after tightening, but requires more physical dexterity and completely releases the motion of the blade, so the alignment method must be more controlled. I found that maintaining a small amount of contact between the other nut and the blade prevented the blade from moving uncontrollably, but still allowed for an appropriate range of motion. Therefore the alignment for one blade is something of an iterative process going between the two sides.

One problem with this setup was the nut not making contact with the blade, because there is no normal force to keep the nut in position while the screw is tightened (it would freely rotate as the screw rotated). Furthermore, when contact is made but the normal force to the blade is not strong, the nut will rotate around unless a tool provides the opposing torque as the screw rotates. The motion of the nut on top of the electrode can itself scratch the gold coating. If the hexagonal nuts' edges are not aligned along the direction of the blade segments, they add extra capacitance between the neighboring electrodes. To solve these issues, I machined a double socket to hold the nuts with the proper orientation and

ensure that there was no scratching from the rotation of the nut on the gold coating during tightening. The double socket is also not deep enough to touch the gold coating itself, and the connecting bar between the two further acts as a block to prevent my glove from touching the blade.
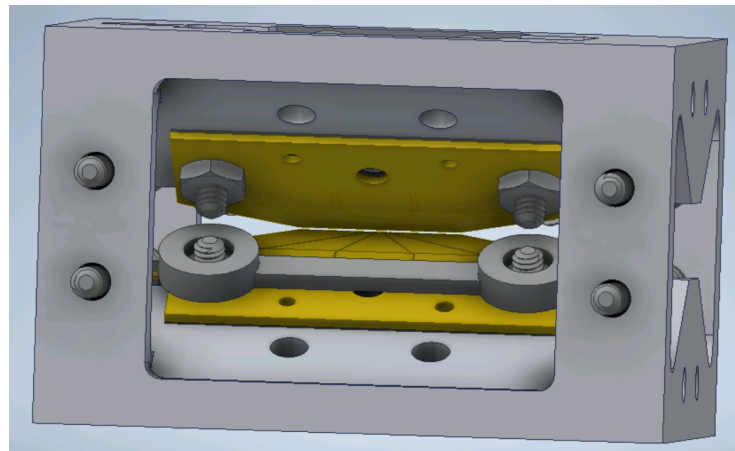

Figure 5.9: Double socket holder

Figure 5.10: Double socket holder limiting the motion of the nuts on the gold coating and blocking the glove from touching the blades closely.

5.3.1 Blade Alignment trial

Using these methods, I performed a trial run of the full blade alignment procedure to see what challenges remain. This was not performed in clean room conditions, but my goal was primarily to test whether any large elements of the procedure were missing or faulty. The test blades I performed this alignment on were not uniform and would not have passed our quality control tests for the final assembly, but they were the closest blades we had at the time since all of the better blades had been broken during previous testing. The primary significance of this comes from the mismatch in the chamfer thickness. Because I align the blade tips by looking at the acute and obtuse pairs, a mismatch in thickness means that the acute and obtuse pairs will have irregular distances. For this reason, as well as the fact that the varied thickness blade plates had not arrived, the true goal of this alignment trial was to test whether just the acute pairs could be aligned to within the tolerance level we desire. Clearly this under-represents the challenges for the final alignment, but this would at least indicate whether the 2.5μm blade alignment would be feasible. I used an Olympus SZX18 microscope to image the blades. A view of the blades during this process can be seen in fig 5.11.
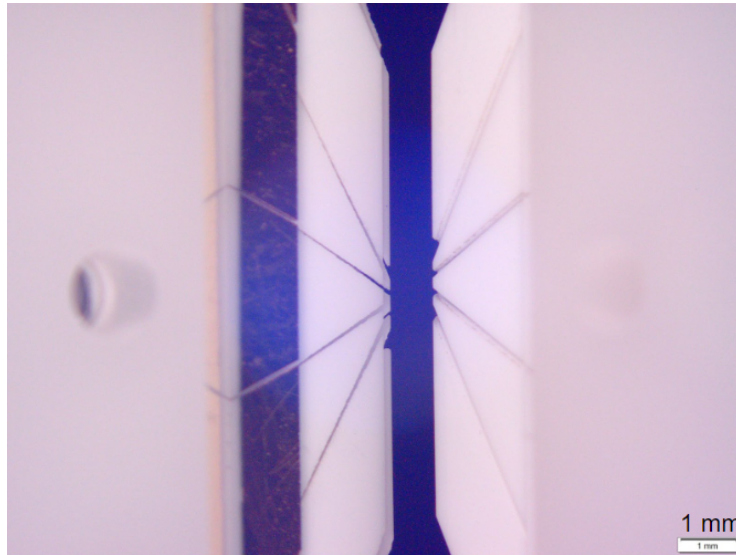

Figure 5.11: View of the blades through a microscope during an alignment procedure. Image taken down the obtuse pair axis.

After using the strategies outlined above, I was able to align the acute pairs to 158 μm and 161 μm. The uncertainty for this measurement is around 1.5μm due to limitations

56

in resolution and determining which pixel is the edge. However, I discovered later that I had used the wrong calibration for the measurement. I acquired a microscope micrometer transparent calibration ruler and recalibrated the pixel-distance measurements. The actual distances for the acute pairs were 211 μm and 215 μm. The obtuse paired angles (corrected for miscalibration factor) were 582 μm and 702 μm. The obtuse pairs are far away from their desired values, illustrating the requirement for thinner blade plates, and the mismatch of the two values despite the similarity of the acute pair distances illustrates the errors in thickness (one blade was very thin, one was very thick, the other two were in tolerable range). However, the process was able to be completed in approximately an hour and a half with a gloved hand, and the alignment of the acute pairs was still aligned with relative uncertainty to within our goal alignment. Therefore, I would consider this preliminary alignment trial to be a success. A more full alignment trial will be completed soon once new blades and blade plates arrive.
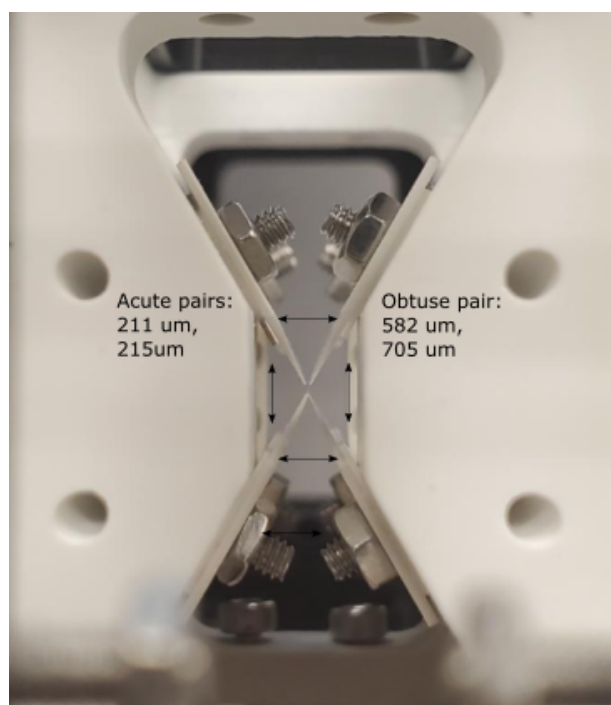

Figure 5.12: Trial alignment values. Relative uncertainties lie within target alignment bounds. Mismatch due to miscalibration of distances during alignment procedure and high obtuse pair values indicate need for thinner blade plates.

5.4 Remaining blade alignment considerations

The last critical error which I have not discussed yet is the blade plane tilt. Unfortunately, this specification was not given directly to the manufacturer, but rather arises out of a complex relationship with a few other dimensions on the spec sheet. Regardless, I plan to accommodate these errors when necessary by applying an equal and opposite tilt to the blade plate using the same micropolishing technique that we use to create the blade dimensions. This process is still in testing, but small tilts of 0.1^o should be possible.

In exploring setups upon which I could eventually perform the final alignment, my original plan was to use one of the microscopes within the University of Waterloo network at the Quantum Nano Center or Research Activity Complex 1 buildings. However, the position of the blades which share an acute angle restricted the working distance I could use for alignment. The 19mm distance to the edge of the blade holder was larger than the working distance for microscopes within this network for higher magnifications. Furthermore, these microscopes would require the blade holder to be vertical, which is an inconvenient orientation for the manual manipulation of the blades since they are not laying flat. Therefore, I decided to build my own custom microscope setup for imaging the blades. For the long working distance objective, I acquired a Mitutoyo objective (Thorlabs MY10X-803) with a 34mm working distance. When paired with a Thorlabs 200mm focal length lens, we can obtain a 10x magnification. The blades will be imaged onto a FLIR camera with a pixel size of 1.2 μm. With this magnification, I should be able to make out displacements below the micron level. The setup will also hold the blade holder at a 30° angle to keep the blade flat, and allow access from the bottom for an allen key to tighten the blades.

While the position of the blades with respect to each other is important for micromotion considerations, the position of the blades with respect to the rest of our system also has significant consequences. Therefore, the exploration of blade alignment must also include the manner in which the blade holder itself (now a reference for the tightened blades) must be aligned to the rest of the chamber. In particular, the high NA Raman axis requires orthogonality of the ion chain to the axis of the Raman optics. I consulted with another student to perform Zemax and Monte-Carlo simulations on the tolerable mismatch of the ion chain. The results affirm that our high NA objective must remain referenced to the stationary window, therefore the ion chain itself has a tolerable angle of 1° with respect to the normal of the Raman beam. In order to further provide control over this angle, I proposed modification of the bridge assembly which attaches the blade holder to the camber. The modified system now has a few degrees of play perpendicular to the Raman axis to ensure that the ion axis is orthogonal.

5.5 Blade alignment results and conclusions

A trial run of the alignment procedure using the tools and methods described above indicates that a full alignment procedure with inter-blade distances to within 5μm of target values is feasible. This trial run also indicated that alignment procedures can be completed in the 1 to 2 hour time-frame, and be clean room compatible with the exception of a finger used for fine control over blade position. This alignment level should prevent micromotion heating from competing with our other cooling methods. Unfortunately, the blade alignment project is still in progress, and won't be complete until the final blades which have been aligned are successfully trapping ions. Further trials on the alignment will be completed soon, as well as tests to ensure that later steps in the vacuum process such as baking and pumping do not interfere with the alignment. The final assembly should be complete before December 2022.

Chapter 6

Summary and Outlook

In this thesis, I have discussed and examined the preparation for running entangling operations on our trapped ions, evaluated the temperature of the ions in our trap, and explored solutions for minimizing a source of heating in our future trap. For what remains, I would like to comment on a few projects which I worked on that have yet to be discussed.

6.1 Raman Upgrade

Since the time when the Raman data presented in this thesis was taken, the Raman system has been upgraded to improve the Rabi rate of our transitions. Recently, we have been obtaining carrier Rabi rates of 100kHz π-time. Because the geometry of our beams has gone from a counter-propagating layout to a perpendicular one, some of the alignment strategies needed adjustment to accommodate a few awkward angles and tight spaces. However, the increase in the Rabi rate has allowed us to see even clearer ion signals, and our Continuous sideband cooling temperature is still very low. The other unknown peaks in the Raman spectrum have not been appearing after the shift in the geometry, which may indicate that the original peaks were an artifact of the counterpropagating design. Furthermore, we are planning to address some of the engineering problems from the previous setup, and implement automated controls wherever possible to reduce daily calibration time. We were even able to see preliminary MS flopping after carefully calibrating the sidebands and detunings. Optimizations are not yet complete, but our quantum information experiments should be in full swing by the end of 2022.

6.2 DMD experiments and loose ends

There were lots of interesting sub-experiments which I was able to contribute to during this time, but which are not included in this thesis. Various system optimizations were explored, from moving our entire setup to a different optical table, to integrating various electronics to our control system, to exploring alternative options for cameras, detection methods, and frequency stabilization systems. I have especially enjoyed contributing to our work using a Digital Micromirror Device (DMD) to implement individual ion addressing. In that work, we demonstrate that through use of a DMD, we can create a Fourier hologram which corrects for aberrations in our system and which yields a spot size capable of reducing intensity cross-talk of neighboring ions to the 1E-4 level. I found the troubleshooting and engineering problems we faced on a daily basis in this project highly engaging. In general, I find that the day-to-day challenges of working in an optics lab have sharpened my problem-solving skills immensely. The periodic debugging process has given me a much more holistic understanding of our experimental apparatus.

References

[1] P. J. Low, "Tolerable experimental imperfections for a quadrupole blade ion trap and practical qudit gates with trapped ions," 2019.

[2] N. Kotibhaskar, "Design and construction of an ion trapping apparatus for quantum simulation experiments," 2019.

[3] R. P. Feynman, "Simulating physics with computers," *International journal of theoretical physics*, vol. 21, no. 6-7, pp. 467–488, 1982.

[4] Y. Wang, M. Um, J. Zhang, S. An, M. Lyu, J.-N. Zhang, L.-M. Duan, D. Yum, and K. Kim, "Single-qubit quantum memory exceeding ten-minute coherence time," *Nature Photonics*, vol. 11, no. 10, p. 646, 2017.

[5] D. Gerlich, *INHOMOGENEOUS RF FIELDS: A VERSATILE TOOL FOR THE STUDY OF PROCESSES WITH SLOW IONS.* None: Wiley And Sons, 2007.

[6] D. Steck, *Quantum and Atom Optics.* Department of Physics, 1274 University of Oregon, Eugene, Oregon 97403-1274: steck.us, 2007.

[7] K. R. Islam, *QUANTUM SIMULATION OF INTERACTING SPIN MODELS WITH TRAPPED IONS.* PhD thesis, University of Maryland, 2012.

[8] K. Mølmer and A. Sørensen, "Multiparticle entanglement of hot trapped ions," *Physical Review Letters*, vol. 82, no. 9, p. 1835, 1999.

[9] P. Lee, *Quantum Information Processing with Two Trapped Cadmium Ions.* PhD thesis, University of Michigan, 2006.

[10] A. Rasmussen, M. D'Onofrio, Y. Xie, J. Cui, and P. Richerme, "Optimized pulsed sideband cooling and enhanced thermometry of trapped ions," *Physical Review A*, vol. 104, no. 043108, 2021.

[11] L. Egan, *SCALING QUANTUM COMPUTERS WITH LONG CHAINS OF TRAPPED IONS*. PhD thesis, Joint Quantum Institute, 2021.

[12] V. M. Sch¨afer, C. J. Ballance, K. Thirumalai, L. J. Stephenson, T. G. Ballance, A. M. Steane, and D. M. Lucas, "Fast quantum logic gates with trapped-ion qubits," *Nature*, vol. 555, pp. 75–78, 2018.

[13] S. Olmschenk, K. Younge, D. Moehring, D. Matsukevich, P. Maunz, and C. Monroe, "Manipulation and detection of a trapped yb+ hyperfine qubit," *Physical Review A*, vol. 76, no. 5, p. 052314, 2007.

[14] D. P. DiVincenzo, "The physical implementation of quantum computation," *Fortschritte der Physik: Progress of Physics*, vol. 48, no. 9-11, pp. 771–783, 2000.

[15] R. Islam, W. Campbell, T. Choi, S. Clark, C. Conover, S. Debnath, E. Edwards, B. Fields, D. Hayes, D. Hucul, I. Inlek, K. Johnson, S. Korenbilt, A. Lee, K. Lee, T. Manning, D. Matsukevich, J. Mizrahi, Q. Quraishi, C. Senko, J. Smith, and C. Monroe, "Beat note stabilization of mode-locked lasers for quantum information processing," *Optics Letters*, vol. 39, pp. 3238–3241, 2014.

[16] C. Senko, *DYNAMICS AND EXCITED STATES OF QUANTUM MANY-BODY SPIN CHAINS WITH TRAPPED IONS*. PhD thesis, University of Maryland, 2014.